

1 **Accounting for Uncertainties in Forecasting Tropical Cyclone-**
2 **Induced Compound Flooding**

3 Kees Nederhoff^{1,2,5}, Maarten van Ormondt¹, Jay Veeramony³, Ap van Dongeren^{2,4}, José A. Á. Antolínez⁵,
4 Tim Leijnse^{4,6}, Dano Roelvink^{2,4}

5 ¹ Deltares USA, 8601 Georgia Ave, Silver Spring, MD 20910, USA

6 ² CURR, UNESCO-IHE Institute for Water Education, P.O. BOX 3015, 2601 DA Delft, The Netherlands

7 ³ Naval Research Lab, Stennis Space Center, MS 39529, USA

8 ⁴ Marine and Coastal Management, Deltares, Boussinesqweg 1, Delft, 2629 HV, The Netherlands

9 ⁵ Delft University of Technology, Stevinweg 1, 2628 CN Delft, The Netherlands

10 ⁶ Institute for Environmental Studies (IVM), Vrije Universiteit Amsterdam, De Boelelaan 1111, 1081 HV Amsterdam, The
11 Netherlands.

12 *Correspondence to:* Kees Nederhoff (kees.nederhoff@deltares-usa.us)

13 **Abstract.** Tropical cyclone impacts can have devastating effects on the population, infrastructure, and on natural habitats.
14 However, predicting these impacts is difficult due to the inherent uncertainties in the storm track and intensity. In addition,
15 due to computational constraints, both the relevant ocean physics and the uncertainties in meteorological forcing are only
16 partly accounted for. This paper presents a new method, called the Tropical Cyclone Forecasting Framework (TC-FF), to
17 probabilistically forecast compound flooding induced by tropical cyclones, considering uncertainties in track, forward speed,
18 and wind speed/intensity. The open-source method accounts for all major relevant physical drivers, including tide, surge, and
19 rainfall, and considers TC uncertainties through Gaussian error distributions and autoregressive techniques. The tool creates
20 temporally and spatially varying wind fields to force a computationally efficient compound flood model, allowing for the
21 computation of probabilistic wind and flood hazard maps for any oceanic basin in the world, as it does not require detailed
22 information on the distribution of historical errors. A comparison of TC-FF and JTWC operational ensembles, both based on
23 DeMaria et al. (2009), revealed minor differences of <10%, suggesting that TC-FF can be employed as an alternative, for
24 example, in data-scarce environments. The method was applied to Cyclone Idai in Mozambique. The underlying physical
25 model showed reliable skill in terms of tidal propagation, reproducing the storm surge generation during landfall and flooding
26 near the city of Beira (success index of 0.59). The method was successfully applied to forecast the impact of Idai with different
27 lead times. The case study analyzed needed at least 200 ensemble members to get reliable water levels and flood results three
28 days before landfall (<1% flood probability error and <20 cm sampling errors). Results showed the sensitivity of forecasting,
29 especially with increasing lead times, highlighting the importance of accounting for cyclone variability in decision-making
30 and risk management.

31

32 1 Introduction

33 Tropical cyclone (TC) induced compound flooding, which occurs when storm surge, heavy rainfall, high tide, and river
34 discharge coincide, can have devastating impacts on coastal communities (Wahl et al., 2015). This type of flooding is
35 particularly concerning as it can result in higher water levels and increased inland flooding, leading to damage and loss of life
36 (e.g., Resio & Irish, 2015). The increased frequency and severity of compound flooding events are expected to worsen due to
37 [climate change including to sea level rise \(e.g., Easterling et al., 2000\)](#), [the effects of climate change changes in extreme storm](#)
38 [surges and wave climates \(e.g., Lin et al. 2012; Mori and Shimura, 2023\)](#), [increased and prolonged precipitation \(e.g., Trenberth](#)
39 [et al., 2003\)](#) as well as on-going coastal development and population growth (e.g. Neumann et al., 2015). Mitigation and
40 preparedness strategies require a sound toolbox for assessing TC-induced compound flooding on coastal communities that
41 enhance short to long-term decision-making.

42
43 Operational and strategic risk analyses are instrumental in analyzing and mitigating potential environmental risks. Operational
44 risk analysis, typically associated with short-term forecasting (~several days), provides immediate response and preparedness
45 for imminent disasters, ensuring the safety and protection of people and property (Roy & Kovordányi, 2012). Conversely,
46 strategic risk analysis focuses on long-term climate variability assessments, delivering insights into hazards and their socio-
47 economic and environmental impacts, thus facilitating informed policy decisions and adaptation strategies (e.g., Nederhoff et
48 al., 2021). Though distinctly different, both perspectives are critical for comprehensive climate risk management, as they offer
49 different scales and timeframes for prevention, preparedness, response, and recovery.

50
51 Forecasting agencies such as the National Hurricane Center (NHC) have significantly improved operational meteorological
52 risk analysis, credited to gains made in numerical weather prediction models (McAdie et al., 2000, Cangialosi et al., 2020).
53 Despite advancements, operational forecast errors remain significant enough to necessitate considering the inherent
54 uncertainties in these forecasts for informed preparedness decision-making (Lamers et al., 2023). A common probabilistic
55 approach is to represent the resulting uncertainty in track prediction by a cone envelope as a graphical representation that
56 illustrates the possible track variation of the TC center (NHC, 2023). The shape of the cone can be derived from the historical
57 error data of the forecast and typically represents a 66.7% probability that the track will be within the cone (i.e., 33.3% chance
58 the track falls outside the cone). The cone increases in size with lead time as the errors in the prediction accumulate. While the
59 cone gives valuable insight into the potential range of TC variability of the core, it can be easily misinterpreted as the
60 corresponding impacted area, which can be substantially larger. Quantification of the uncertainty in track prediction can be
61 computed with several methods. For example, De Maria et al. (2009) introduced a Monte Carlo method to generate 1,000
62 realizations by randomly sampling from historical error distribution functions from the past 5 years for both the track and
63 intensity. De Maria et al. (2013) improved their method so that the track uncertainty is estimated on a case-by-case basis using
64 the Goerss predicted consensus error (GPCE; Goerss, 2007), where the uncertainty is estimated based on the spread of a

65 dynamical model ensemble instead of historical averages. Other methods exist ~~and~~ ~~for~~ ~~example~~; Chen et al. (2023)
66 introduced a deep-learning ensemble approach for predicting tropical cyclone rapid intensification. However, these methods
67 were all derived to provide insight, before landfall, into the uncertainty of the wind speeds and not designed to force
68 hydrodynamic or wave models; and can thus result in too erratic forcing conditions.

69
70 Early Warning Systems (EWS) for coastal compound flooding are sensitive to uncertainties in the TC, including nonlinear
71 interactions between the TC size, forward speed, location of landfall, tides, rainfall, and infiltration. However, often EWS for
72 coastal flooding use physics-based and, due to computational constraints, deterministic approaches in which the best track is
73 used to force a hydrological & hydrodynamic model that computes the storm surge and the complex interactions between
74 coastal, fluvial, and pluvial processes. ~~For example, the~~ ~~(e.g.)~~ Global Storm Surge Information System ~~(GLOSSIS)~~ ~~is~~ based
75 on Delft3D Flexible Mesh ~~(Kernkamp et al., 2011)~~ ~~and runs operationally 4 times daily to produce 10-day water level and~~
76 ~~storm-surge forecasts for the entire globe. GLOSSIS is typically forced with NOAA's GFS forcing although there is also~~
77 ~~functionality in place to use hurricane tracks. Another example is the~~ ~~and~~ Coastal Emergency Risks Assessment ~~(CERA)~~
78 based on ADCIRC ~~(Luettich et al., 1992)~~. ~~CERA is an effort to provide operational advisory services related to impending~~
79 ~~hurricanes in the United States only and uses the NHC official advisory every 6 hours. Neither GLOSSIS nor CERA accounts~~
80 ~~for uncertainties in the meteorological forcing.~~

81
82 Several examples of probabilistic coastal flood methods ~~do~~ capture uncertainty in forcing. For example, the Global Flood
83 Awareness System (GloFAS; Alfieri et al., 2013) is a modeling chain run by the European Centre for Medium-Range Weather
84 Forecasts (ECMWF) based on the LISFLOOD hydrological model forced by 51 ensemble members. While GloFAS is an
85 excellent resource for communities worldwide, it operates at a large scale with a relatively coarse resolution of 0.1 degrees
86 (~10 km), ~~and~~ is thus not designed explicitly for TCs that require high spatial resolutions (Roberts et al., 2020), and neither
87 account for relevant coastal processes such as tides. Higher resolution and the inclusion of coastal processes can be found in
88 several regional applications. For example, the Stevens Flood Advisory System (SFAS; Ayyad et al., 2022) is an ensemble-
89 based probabilistic forecasting of tide, surge, and riverine flow across the US Mid-Atlantic and Northeast coastline and runs
90 for 96 different atmospheric forcing datasets. Other examples include forecasting systems from the UK Met Office (Flowerdew
91 et al., 2010) and the Royal Netherlands Meteorological Institute (de Vries, 2009). All these systems rely on coarser numerical
92 forecasting products, focus on mid-latitude regions, and are thus not explicitly designed to forecasts hazards related to TCs.

93
94 Probabilistic modeling systems for TC-induced coastal flooding for operational risk analyses in the US and Japan ~~include~~
95 ~~Pinclude~~ P-Surge (Taylor and Glahn, 2008; Gonzalez and Taylor, 2021), which uses data from the NHC to create a set of
96 synthetic storms by perturbing the storm's position, size, and intensity based on past errors of the advisories. Subsequently, the
97 Sea, Lake, Overland, Surge from Hurricanes model (SLOSH; Jelesnianski 1992) is run and forecasts storm surge in real-time

98 when a hurricane is threatening. However, SLOSH does not account for several relevant (coastal) processes (e.g., tides, waves,
99 rainfall, infiltration) and thus lack their interactions. The Japan Meteorological Agency (JMA) does use a dynamic tide and
100 storm surge model (Higaki et al., 2009) but only accounts for a limited number of 11 ensemble members (Hasegawa et al.,
101 2015). Moreover, both methods are created with a specific region in mind and are not easily transferable to other locations.

102

103 Besides probabilistic physics-based techniques, statistical machine-learning techniques (e.g., Lecacheux et al., 2021 or Nguyen
104 & Chen, 2020) are becoming increasingly popular in reducing the computational expense of forecasting compound flooding.
105 However, these machine learning downscaling methods lack nonlinear interactions between relevant coastal processes driving
106 compound flooding. Hybrid methods focus on reducing the number of tracks simulated and proved capable of accurately
107 representing a larger set of scenarios (Bakker et al., 2022).

108

109 As introduced by Suh et al. (2015), the constraints in real-time forecasting for operational risk analysis are around both
110 'accuracy' and 'promptness'. In other words, the time constraints associated with forecasting dictate that some modeling systems
111 use a purely deterministic approach or a limited number of ensemble members to perform more detailed compound flooding
112 predictions and thus simplify the meteorological uncertainty (e.g., GLOSSIS, CERA, JMA). On the other hand, probabilistic
113 approaches for meteorology with a large number of ensemble members use simplified hydrodynamics or have an insufficient
114 resolution for TCs and thus do not account for the processes needed to forecast TC-induced coastal compound flooding (e.g.,
115 GloFAS, SFAS, NHC). In summary, the current shortcomings of existing methodologies include the lack absence of high-
116 resolution models specifically tailored for analyzing coastal compound flooding. Additionally, there is a notable deficiency in
117 probabilistic assessments of tropical cyclone flooding that incorporate the uncertainties inherent in forecasting cyclone tracks.
118 Moreover, there is a need for a universally applicable methodology that can be seamlessly adapted to various case studies
119 globally.

120

121

122 To address the limitations listed, we propose a method to generate probabilistic wind and compound flood hazard maps by
123 using, for the first time, ensembling techniques via statistical emulation of TCs combined with physics-driven modeling for
124 coastal compound flooding. The workflow emulates the TC evolution using an autoregressive technique in combination with
125 reported mean errors in track and intensity, similar to DeMaria et al. (2009) but without the need for historical error distribution
126 functions. Next, this emulator produces an ensemble of several (herein thousands) TC members. Then, for each ensemble
127 member, a time- and spatially-varying wind field is generated and used to force a computationally efficient compound flood
128 model SFINCS (Leijnse et al. 2021). The output consists of probabilistic wind and flood hazard maps that can be forecast on
129 time with limited computational resources anywhere in the world. This paper refers to the TC forecasting framework as the
130 Tropical Cyclone Forecasting Framework, TC-FF.

131

132 The paper is structured as follows. Section 2 introduces the Monte Carlo forecasting methodology. Section 3 describes the
133 case study site and historical event of interest. The materials and methods used in this paper are described in Section 4.
134 Validation in terms of tides and storms and application of the forecasting methodology are presented in Section 5. Finally,
135 Sections 6 and 7 discuss and summarize the main conclusions of the study.

136 2 Tropical Cyclone Forecasting Framework

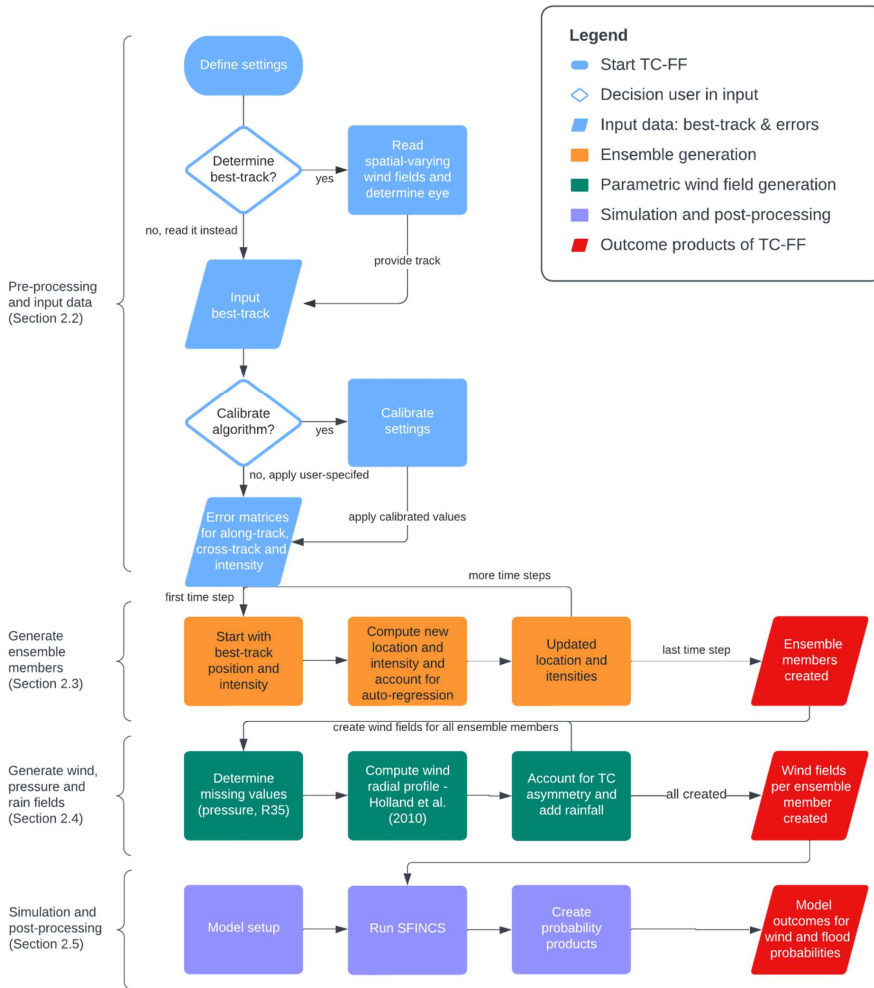
137 In this paper, we introduce the probabilistic Tropical Cyclone Forecasting Framework, TC-FF, to compute TC-induced
138 compound flooding for operational risk analysis. Our approach integrates a TC emulator using a Monte Carlo-based ensemble
139 sampling generation with an autoregressive technique, which is a simplified adaptation of DeMaria et al. (2009). The ensemble
140 members are generated around the forecasted official track, considering the average historical errors in intensity, cross-track,
141 and along-track. [We deem these variables as the primary source of track uncertainty \(e.g. Fossell et al., 2017\). Other variables](#)
142 [\(e.g. information on wind radii\) can be \(stochastically\) correlated to them.](#) The ensemble members are provided as input for
143 the fast compound flood model called SFINCS. Additionally, TC-FF considers tidal movements, storm surge, precipitation,
144 and infiltration. The outcomes are consolidated into a unified probability product. By choice, each member has an equal
145 likelihood of occurrence. The Python code for this method is accessible on GitHub via the following link:
146 https://github.com/Deltares-research/cht_cyclones or <https://github.com/Deltares/CoastalHazardsToolkit>. one is referred to
147 [Zenodo \(Nederhoff & van Ormondt, 2023\)](#)

148 2.1 TC-FF flowchart

149 A compact flowchart of TC-FF used to generate the ensemble member is shown in [Figure 1](#)~~Figure 1~~. The steps of this process
150 are as follows:

- 151 1. **Define settings:** The user specifies the data source, period, time step of the ensemble generation, and the number of
152 ensemble members requested.
- 153 2. **Input best track:** The code either determines the best track based on gridded time and spatial-varying wind and
154 pressure fields (e.g., COAMPS-TC; Doyle et al., 2014) or reads in the forecasted track by one of the forecasting
155 centers (e.g., NHC or other agencies).
- 156 3. **Error matrices for along-track, cross-track, and intensity:** The tool first computes random realizations based on
157 the along-track, cross-track, and intensity standard deviations imposed for the time steps requested. The imposed
158 mean absolute error is scaled with the timestep to overcome any time step dependency.
- 159 4. **Generate ensemble members:** Following the approach of DeMaria et al. (2009), a Monte Carlo method generates
160 numerous ensemble members based on error matrices of the previous step in combination with an autoregressive
161 technique for the along-track, cross-track, and intensity error.

- 162 5. **Generate wind, pressure, and rain fields:** Generate meteorological forcing conditions, i.e., the surface wind and
163 pressure fields per time step per ensemble member, based on parametric methods (e.g., Holland et al., 2010) for
164 subsequent analysis and application within numerical models. Rainfall can be included as well via intensity
165 relationships.
- 166 6. **Simulation and post-processing:** In this study, the compound flood model SFINCS is applied, but in principle, other
167 hydrodynamic models can also be applied, albeit typically at a higher computational expense. Data from the different
168 ensembles are combined into several probabilistic outputs ranging from the probability of gale force winds (wind
169 speed > 35 knots or >18 m/s), compound flooding (water depth > 15 cm) to quantile estimates (e.g., 1% exceedance
170 water level).
171



172

173 **Figure 1. Flowchart of the Tropical Cyclone Forecasting Framework (TC-FF). Pre-processing stages are represented in light blue,**
 174 **the computational core of ensemble generation is denoted in orange, the parametric wind field generation is portrayed in green, the**
 175 **hydrodynamic simulation and analysis of winds are marked in purple and outcomes in red.**

176 In the subsequent paragraphs, we describe in more detail the pre-processing, the computation of the ensemble members (track
177 and intensity variations), and the determination of time- and spatially-varying wind fields.

178 2.2 Pre-processing and input data

179 The pre-processing of TC-FF comprises three components.

180

181 First, one specifies the period they would like to simulate, including the total time period over which wind fields need to be
182 generated and the time period over which the ensembles need to be generated. In addition, a timestep for ensemble generation
183 (default 3 hours) needs to be specified. At this stage, one also specifies the mean absolute error and auto-regression coefficients
184 for the along-track, cross-track, and intensity. When these values are unknown, calibration needs to be performed to determine
185 them by comparing them with the reported errors of the forecast center (see calibration in Section 5.2.1). At this stage, one
186 also specifies the number of ensemble members requested. The influence of the number of ensemble members is discussed in
187 Section 5.3.2.

188

189 Second, since TC-FF creates random realizations around the best track, an input track is needed. Depending on the application,
190 TC-FF reads a forecast bulletin that generates the track or ~~determined~~determines the best track from the output of a high-
191 resolution regional meteorological model. The determination of a track from a meteorological model is based on an algorithm
192 that finds the minimum pressure in an area of interest. It takes in grid values, u and v wind components, pressure, minimum
193 distance for clustering, and returns lists of x and y coordinates of cyclone eyes, the maximum wind speed plus pressure around
194 each eye.

195

196 Third, before the generation of the ensemble members, TC-FF creates random errors with a normal distribution based on the
197 provided average errors. Matrices are two-dimensional, with one dimension being the number of time stamps and the other the
198 number of ensemble members. The imposed mean absolute error is scaled with the timestep to overcome any time step
199 dependency and converted into a standard deviation.

200 2.3 Ensemble members

201 2.3.1 Track realizations and calibration

202 An important component in TC-FF is the generation of track realizations (or ensemble members) from the official track
203 forecast. The official positions are interpolated with a spline function to include values at all requested times. Our approach
204 for the track realization largely follows DeMaria et al. (2009). We decompose the track error into the along-track (AT) and
205 cross-track (CT) components and account for the track error serial correlation via autoregressive regression (Equations 1 and
206 2).

$$AT_t = a_t AT_{t-i} + B_{rnd} \quad \text{Equation 1}$$

$$CT_t = c_t CT_{t-i} + D_{rnd} \quad \text{Equation 2}$$

207 in which AT_t and CT_t are the AT and CT error at time steps t , a_t and c_t are constants, AT_{t-3} and CT_{t-3} are errors of the previous
208 time step (typically $i=3$ hours), and B and D are random numbers that are normal (Gaussian) distributed, scaled with the mean
209 absolute error but are limited to $\pm 2\sigma$.

210

211 Unlike DeMaria et al. (2009), we do not access the probability distributions of historical errors. Instead, we calibrate the
212 parameters (a_t , c_t , and mean absolute errors for B and D) based on the reported historical errors from the agency responsible
213 for the issued forecast (see Section 5.2.1). This is a simpler methodology and requires substantially less data (which is also
214 typically not accessible outside the forecast centers). These historical errors are routinely reported by the forecast centers (e.g.,
215 see Section 4.1.2 for information on the data sources used in this paper). Note that errors in our implementation (neither the
216 error nor the auto-regressive coefficient) vary with lead time. We calibrate a constant mean absolute error in combination with
217 a single auto-regression coefficient (see Section 5.2.1 for calibration and Section 5.2.2 for the influence of simplifications).
218 Moreover, the mean absolute error is converted into a standard deviation using a fixed relationship assuming a normal
219 distribution of the error and scaled with the applied time step to allow the user flexibility in the applied time step.

220

221 The determination of the ensemble members is subsequently based on the sum of the forecast and random error components.
222 In other words, we add the along-track and cross-track error to forecasted along- and cross-track. An example of the first 20
223 ensemble members is presented in [Figure 2](#) ~~Figure 2~~B. Using this procedure, 10,000 ensembles are generated for each forecast
224 case within this study; however, it is possible to use fewer ensemble members to reduce the computational cost but at larger
225 statistical uncertainty (see Section 5.3.2 for trade-offs).

226 2.3.2 Intensity realizations and calibration

227 Similar to the track realization, the maximum wind speed (intensity) at a specific interval is determined using a random
228 sampling approach. The starting point is the official forecast of intensity that is interpolated to include values at all requested
229 times, and a random error component (VE_t) is added.

$$VE_t = e_t VT_{t-3} + F_{rnd} \quad \text{Equation 3}$$

230 in which VE_t at time steps t , e_t is a constant, VE_{t-3} are errors of the previous time step (typically 3 hours) and F is random
231 numbers that are normally distributed, scaled with the mean absolute error and is limited to $\pm 2\sigma$.

232

233 The inland wind decay model adjusts the maximum intensity as a function of the distance inland, is directly based on DeMaria
234 et al. (2009) and is computed with Equation 4. If the intensity of any inland ensemble member exceeds this predetermined
235 value at any forecast time, the intensity is adjusted to match this value. Subsequently, the intensity errors are recalculated based

Formatted: Font: 10 pt, Not Bold

Field Code Changed

Formatted: Font: 10 pt, Not Bold

Field Code Changed

236 on the adjusted intensity. Additionally, if the intensity of an inland ensemble member falls <7.7 m/s (15 knots) at any point in
237 time, the TC intensity is reset to zero for all subsequent periods to overcome any unrealistic reintensifying TCs. All these
238 criteria follow DeMaria et al. (2009).

$$V_i = 20 + 120e^{0.0035D} \quad \text{Equation 4}$$

239 in which the maximum wind speed (V_i) in knots and the distance to land (D) in kilometers (with negative values indicating
240 inland cyclones) are given, the intensity of an inland cyclone can be determined.

241

242 The intensity implementation differs from DeMaria et al. (2009) in the following ways. We remove the dependency that the
243 error scales with wind intensity and bias correction. Again, the determination of the ensemble members is based on the sum of
244 the forecasted and random components computed with Gaussian mean absolute errors and an auto-regressive constant over
245 lead time. Similar to the track realization, intensity errors are scaled with the time step to overcome any time step dependency.
246 The influence of the simplifications and the difference compared to NOAA operational code based on the original DeMaria et
247 al. (2009) and DeMaria et al. (2013) implementation are discussed in Section 5.2.2.

248 2.4 Parametric wind fields

249 After the determination of the ensemble members, the time and spatial varying wind fields are constructed and written in a
250 polar coordinate system. Several (horizontal) parametric wind profiles have been presented in the literature (e.g., Fujita, 1952;
251 Chavas et al., 2015), with the original Holland wind profile (Holland, 1980) being the most widely used due to its relative
252 simplicity. Several codes have been developed for storm surge models to provide time and spatial wind and pressure fields
253 (e.g., Hu et al., 2012 for ADCIRC). Deltares has developed the Wind Enhance Scheme (WES; Deltares, 2018) to generate TC
254 wind and pressure field around the specified location of a tropical cyclone center and given a number of TC parameters. In its
255 current implementation, information on wind radii (radius of gale force winds) can be considered in the Holland et al., (2010)
256 formulation using information either from best track-data or from the proposed relationships of Nederhoff et al. (2019), which
257 increases the accuracy of the method. Furthermore, the asymmetry of the wind field in a TC is also implemented, as delineated
258 by Schwerdt et al. (1979). [Winds throughout this study are converted from 1-minute to 10-minute using a conversion factor
259 equal to 0.93 \(Harper et al., 2010\).](#) Additionally, tropical cyclone-induced precipitation can be incorporated using empirical
260 relationships such as IPET (2006).

261 2.5 SFINCS simulation and post-processing

262 After the determination of the wind fields for all the requested ensemble members, TC-FF runs a hydrodynamic model. In this
263 study, we apply the compound flood model SFINCS (Leijnse et al., 2021), which lends itself well to a large number of
264 simulations in a reasonable amount of time due to its reduced complexity. SFINCS reads the tidal boundary conditions and
265 wind, pressure, and rainfall conditions from the wind fields. Once all the ensemble member simulations have finished,

Formatted: Font: 10 pt, Not Bold

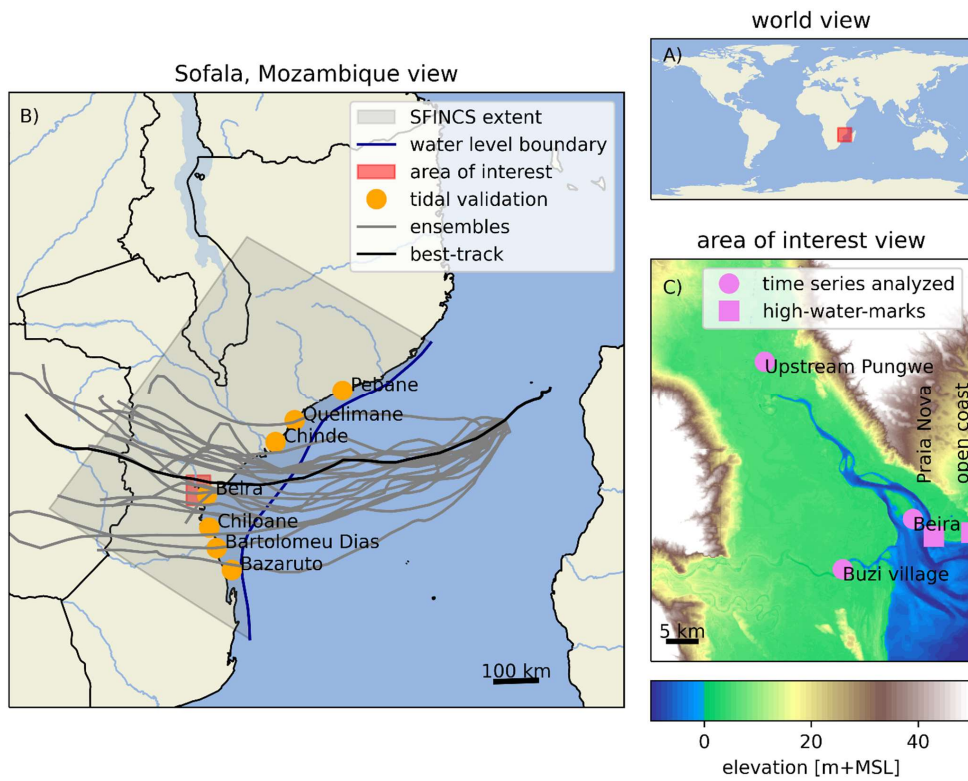
Field Code Changed

266 probability products regarding wind and flood hazards are created. These products are created by sorting the results for each
267 grid cell and providing estimates for either specific intervals (e.g. wind speeds > 35 knots or water depth > 15 cm) or quantile
268 estimates (e.g., 1% exceedance water level). Only track uncertainty is considered in these estimates.

269 3 Case study

270 The TC forecasting framework is applied to a historical event that took place in Mozambique's Sofala province: Cyclone Idai,
271 in March 2019. Mozambique is a country located in southeastern Africa (Figure 2~~Figure-2~~A). The country has a diverse
272 population of over 31 million people, of which 2 million live in the Sofala province in central Mozambique (National Institute
273 of Statistics of Mozambique, 2017). Sofala is primarily rural, with small communities along the Pungwe and Buzi river deltas
274 (Emerton et al., 2020). Beira is the province's largest city, home to over 500,000 people, and an important port linking the
275 hinterland to the Indian Ocean. The city is prone to flooding, particularly during the rainy season, which generally extends
276 from October to April or May. This period coincides with the cyclone season, as cyclones often bring intense rainfall to the
277 region. The vulnerability of Beira to flooding is exacerbated by factors such as climate change, rapid urbanization, and limited
278 infrastructure.

279
280 Cyclone Idai was an example of a compound flood event that affected large parts of the coastal delta of Sofala (Eilander et al.,
281 2022). The storm began as a tropical depression in the Mozambique Channel, causing extensive flooding after its first landfall
282 in early March. It later intensified as it moved back over the sea, developing into a tropical cyclone with 10-minute sustained
283 wind speeds of 165 km/h. Idai made landfall near the port city of Beira, bringing powerful winds, resulting storm surge, and
284 heavy rains that caused widespread flooding and destruction. Large areas were flooded, first around the coast and a few days
285 later, more inland in the Buzi and Pungwe floodplains. The total rainfall across the five days from March 13-18 ranged from
286 250–660 mm (NASA GPM, 2019). Over 112,000 houses were destroyed, and an estimated 1.85 million people were affected
287 (UN OCHA, 2019).



288

289 **Figure 2.** View of the study site: (A) Mozambique's Sofala Province is situated in the southeastern region of Africa in the Southern
 290 Hemisphere. (B) Geographical and hydrodynamic representation of the study area. The SFINCS model extent, highlighted in Panel
 291 B, encompasses a portion of the Sofala region, forced offshore with a water level boundary, and is validated at seven tidal stations
 292 (indicated by orange circles; see Section 8.1). The best track is represented by a solid dark line, with the first 20 ensemble members
 293 5 days before landfall demonstrated as gray lines. (C) The area of interest is the Pungwe estuary, situated near the city of Beira.
 294 Model validation also takes place at two high-water-marks close to the city (signified by a purple box), with model outcomes depicted
 295 at three diverse locations across the estuary (marked by circles).

296

297 4 Material and methods

298 4.1 Materials

299 4.1.1 Elevation datasets

300 Several topographic and bathymetric datasets were collected and combined to develop a merged DEM. Data includes field
301 survey data points collected during three campaigns in November-December 2020 across Beira, locally-collected LiDAR [with](#)
302 [a resolution of 2 meter](#), bathymetric charts, MERIT (Yamazaki et al., 2017; [90 meter](#)) and GEBCO19 (IOC, IHO and BODC,
303 [2003; 450 meter](#)). Careful consideration was given to prioritize specific datasets in space to ensure the most detailed, recent,
304 and accurate datasets were used in a given area. For example, survey and LiDAR data is bare earth and prioritized over the
305 usage of MERIT and GEBCO19. The merged DEM was produced on medium-resolution (50 m) regional DEM, and a fine-
306 resolution (5 m) local DEM in Beira. For more information on merging the data, one is referred to Deltares (2021).

307 4.1.2 Forcing conditions

308 Tidal boundary conditions were based on harmonic constituents provided by TPXO 8.0 (Egbert and Erofeeva, 2002), and tidal
309 amplitudes and phases for all available 13 components were applied. The best track data (BTD) by the Joint Typhoon Warning
310 Center (JTWC) is used throughout this study for meteorological forcing conditions (JTWC, 2022). Reported error statistics by
311 the JTWC for the 5-year average from 2016-2020 were used to inform the ensemble generation (JTWC, 2021). Ensemble
312 members from TC-FF were compared to 1,000 members produced with the code from NOAA, NHC, and JTWC based
313 DeMaria et al. (2009) and DeMaria et al. (2013) that is used operationally (Buck Sampson, personal communication; June 5,
314 2023).

315 4.1.3 Validation data

316 Observed tidal coefficients near the city of Beira were used for the calibration and validation of the model (van Ormondt,
317 2020; see [Figure 2](#) for locations). The validation of the event Cyclone Idai (2019) consisted of comparing both,
318 observed and modeled flood extent in deltas of the Pungwe and Buzi rivers and high-water marks in the city of Beira. The
319 observed flood extent was derived from Sentinel-1 synthetic aperture radar data (Eilander et al., 2022); and two observed high
320 water marks (Deltares, 2021) were used, one at Praia Nova, in the western side of the city, and another one at the open coast
321 beach in the southeast (see [Figure 2](#) for locations). Correspondingly, values of modeled flood extent and high water
322 marks were output at the same locations.

323 4.2 Methods

324 4.2.1 Area schematization

325 For this study, we employed the Super-Fast INundation of CoastS (SFINCS) model, which solves the simplified equations of
326 mass and momentum for overland flow in two dimensions (Leijnse et al. 2021). The goal was to create one continuous
327 compound flood area model that computes tidal propagation, storm surge, pluvial and fluvial flooding.

328

329 The area schematization builds upon Eilander et al. (2022) but varied in three ways. First, we extended the model alongshore
330 and in deeper water to alleviate the need to nest in a large-scale regional coastal circulation model and generate tidal
331 propagation and storm surge within the domain. The model was extended ~500 km alongshore from Beira to ensure that a
332 cyclone hitting Beira is fully resolved within the domain. Moreover, the model was extended into 1000-meter water depth
333 where wind shear has a negligible impact on the storm surge. Using a quadtree implementation (e.g., Liang et al. ,2008), we
334 applied a variable model resolution ranging from 8000 to 500 meters. A quadtree is a technique in which the refinement from
335 one level to another is based on the original cell but divided into 4 smaller cells with 2 times smaller grid size and allows
336 extending the model setup into deeper water without having time step restrictions in deeper water based on the explicit
337 numerical scheme of SFINCS. Second, high-resolution topo-bathymetry and land roughness were included in the native
338 resolution utilizing sub-gridsubgrid lookup tables (Leijnse et al., 2020). However, the hydrodynamic computations were
339 performed on a coarser resolution to save computational time. Up to 10-meter DEM information was included in the 500-
340 meter grid cells (i.e., factor 50 refinement). Lastly, sub-gridsubgrid bathymetry features were included to account for maximum
341 dune height based on the DEM to control overflow during storm conditions around Beira. For both the subgrid lookup tables
342 and features, the elevation datasets from Deltares (2021) on the 5-meter resolution were used (see Section 4.1.1 for more
343 information). For the lookup tables, we linearly interpolated the high-resolution DEM onto the subgrid. For the subgrid
344 features, the lines element had a resolution of 500 meters and per vertices, the highest point in a radius of 500 meters was used.

345

346 A spatially-varying roughness and infiltration was used based on land elevation. All points above mean sea level (MSL) have
347 a high Manning friction coefficient of $0.06 \text{ s/m}^{1/3}$, and an infiltration rate of 1.9 mm/hr (typical values from HSGs Group C;
348 United States Department of Agriculture, 2009), and all other points have lower friction of $0.02 \text{ s/m}^{1/3}$ to represent water and
349 do not have any infiltration. The SFINCS model was forced with tidal boundary conditions and time- and spatially-varying
350 winds, pressure, and rainfall fields. At the offshore boundary, tidal water levels were imposed and inverted barometer effect
351 accounted for. We refer to Section-Appendix 8.1 for calibration of the tides, in which we show that the area model reproduces
352 tides with a median MAE of 21 cm. Wind and pressure fields were created with the Holland wind profile (Holland et al. 2010)
353 based on the BTD (see Section 2.4 for details). Rainfall for TCs was based on the Interagency Performance Evaluation Task
354 Force Rainfall Analysis (IPET, 2006) method. Comparison with the reported rainfall total revealed a significant
355 underestimation of cumulative rainfall during Idai based on IPET. Based on the magnitude of the underestimation, rainfall

356 estimates by IPET were tripled, resulting in a cumulative rainfall in the area of interest of 495 mm for the best track, which is
357 in a similar order of magnitude as observed (see Section 3). For fluvial processes, rather than using data sources like river
358 discharge measurements or a hydrological model, our model only relies on a rain-on-grid with infiltration methodology to
359 simulate surface runoff and its subsequent accumulation, thus providing a first-order estimate of fluvial flooding.

360 4.2.2 Simulations periods

361 The validation of the area schematization focused on two time periods. First, 3 spring-neap cycles (January 13, 2022, until
362 February 26, 2022) were used for the tidal calibration and validation in the area of interest (see Appendix 8.1). Second, Idai
363 was hindcasted forced with the JTWC BTD and compared to observational data for flood extent and high-water levels (Section
364 5.1). After validation of the area schematization, the new forecasting methodology introduced in Section 2 was applied. Various
365 lead times ranging from 1 to 5 days before the second landfall for 10,000 ensemble members were computed (Section 5.3).

366

367 Model runs were performed on the Deltares Netherlands Linux-based High-Performance Computing platform using 10 Intel
368 Xeon CPU E3-1276 v3. The simulations were run on a CPU with openMP enabled to utilize the 4 cores per Xeon processor.
369 On average, a 7-day Idai simulation took about 4 minutes on a single coreprocessor. Running all 50,000 events took ~15 days
370 using all 10 processors (or 40 cores).

371 4.2.3 Model skill

372 Several accuracy metrics were calculated throughout this study: model bias, mean-absolute-error (MAE; Equation 5Equation
373 5), root-mean-square-error (RMSE; Equation 6Equation-6), unbiased RMSE (uRMSE; RMSE with bias removed from the
374 predicted value). These error metrics are used for comparison in water levels, wind speed and track errors.

Formatted: Check spelling and grammar

Formatted: Check spelling and grammar

$$MAE = \frac{1}{N} \sum (|y_i - x_i|) \quad \text{Equation 5}$$

$$RMSE = \sqrt{\frac{1}{N} \sum (y_i - x_i)^2} \quad \text{Equation 6}$$

375 where N is the number of data points, y_i is the i-th prediction (modeled) value, x_i is the i-th measurement.

376

377 Moreover, skill is quantified by binary flood metrics (Wing et al. 2017). The model output (M) is converted to one of two
378 states: wet (1) or dry (0), using a commonly used threshold of 15 cm (e.g., Wing et al. 2017) and compared to the Sentinel
379 benchmark data (B). The Critical Success Index (C; Equation 7Equation-7) accounts for both overprediction and

Formatted: Font: Not Bold, Check spelling and grammar

380 underprediction and can range from 0 (no match between modeled and benchmark data) to 1 (perfect match between modeled
381 and benchmark data).

$$C = \frac{M_1 B_1}{M_1 B_1 + M_0 B_1 + M_1 B_0}$$

Equation 7

Formatted: Font: 10 pt, Not Bold

Field Code Changed

382

383 For the comparison of cumulative distribution functions (CDF) of cross-track, along-track and intensity, we also applied the
384 Continuous Ranked Probability Score (CRPS; Matheson & Winkler, 1976). CRPS measures how good forecasts are in
385 matching observed outcomes; where CRPS = 0, the forecast is wholly accurate, and CRPS = 1, the forecast is wholly
386 inaccurate.

$$CRPS(F, x) = \int_{-\infty}^{\infty} [F(y) - F_0(y)]^2 dy$$

Equation 8

Formatted: Font: 10 pt, Not Bold

Field Code Changed

387 where F(y) is the CDF is associated with an empirical probabilistic reference and prediction.

388 4.2.4 Analysis method

389 The analysis of forecasting results was undertaken using several methods. Initially, extreme wind speeds and water levels were
390 assessed by charting them as time-series data, inclusive of quantile estimates such as the 95% confidence interval (CI).
391 Following this, the maximum values registered during the simulation were organized into cumulative distribution functions
392 (CDFs). This process offered insights into their exceedance probability. Finally, the mean probability of flooding was
393 computed. The method to derive this value entailed counting the instances where computational cells registered a minimum of
394 15 cm of water. Only cells positioned above mean sea level (MSL) were incorporated into the area estimates.

395 **5 Results**

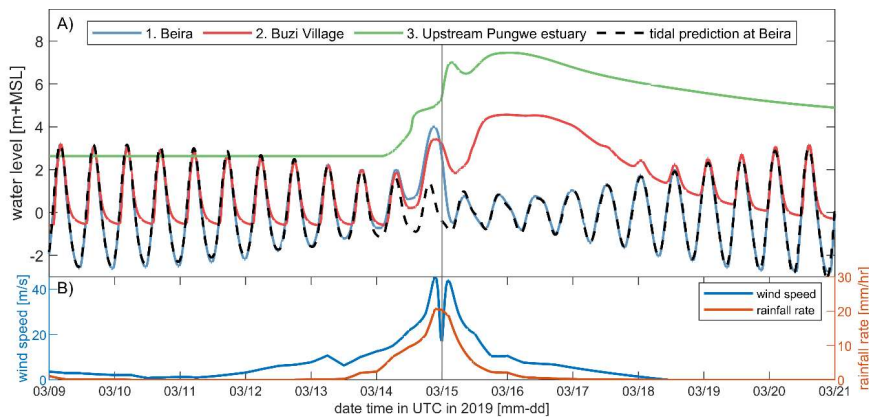
396 This section is organized into three parts, each addressing a crucial aspect of our study on Cyclone Idai's compound flooding.
397 First, we assess the model's accuracy in simulating tidal, storm surge, and combined pluvial and fluvial impacts (Section 5.1).
398 Next, calibration of TC-FF to average errors for the along-track, cross-track, and intensity for the Southern Hemisphere and
399 validation of TC-FF for Idai specifically to the implementation from NOAA, NHC and JTWC that are used operationally is
400 presented (Section 5.2). Lastly, we delve into forecasting uncertainties and their effects on flood predictions, using ensemble
401 simulations with various lead times (Section 5.3).

402 **5**

403 **5.1 Verification of the numerical model for Cyclone Idai**

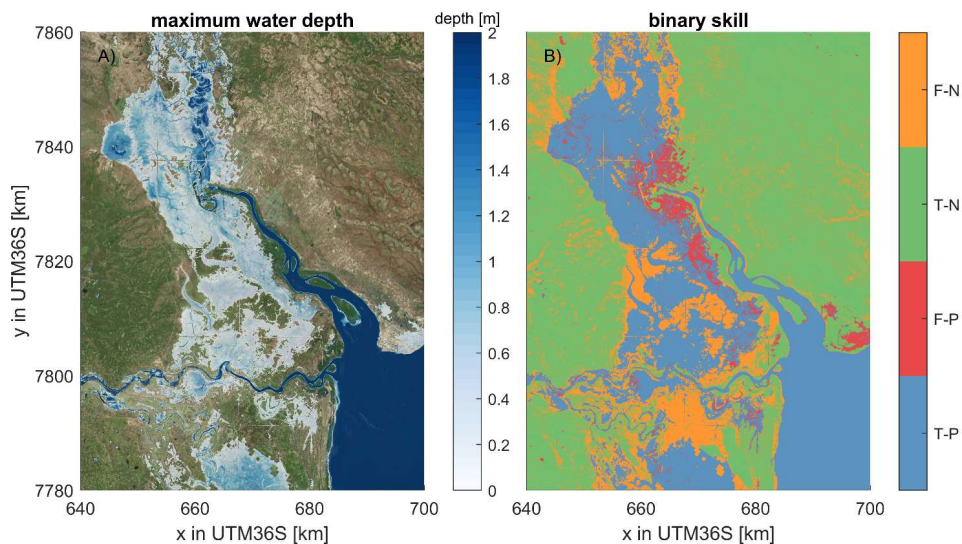
404 Computed water levels near Beira show the strong tidal modulation and the wind-induced storm surge during the landfall of
405 the cyclone (Figure 3 – panel A; blue line for water level and vertical line for moment of landfall). Based on the
406 difference between the predicted astronomic tide and the total modeled water level, we estimate a storm surge of >3.5m due
407 to the ~45 m/s wind speeds (Figure 3 – panel B). The storm surge at Beira is driven by wind setup as well as pluvial
408 and fluvial drivers. Deeper in the estuary, in the Pungwe flood plains, water levels peaked several days after landfall due to
409 intense upstream rainfall and subsequent runoff. Water levels near Buzi Village seem to be a combined result of first marine
410 and second riverine-driven water levels.

Formatted: Normal

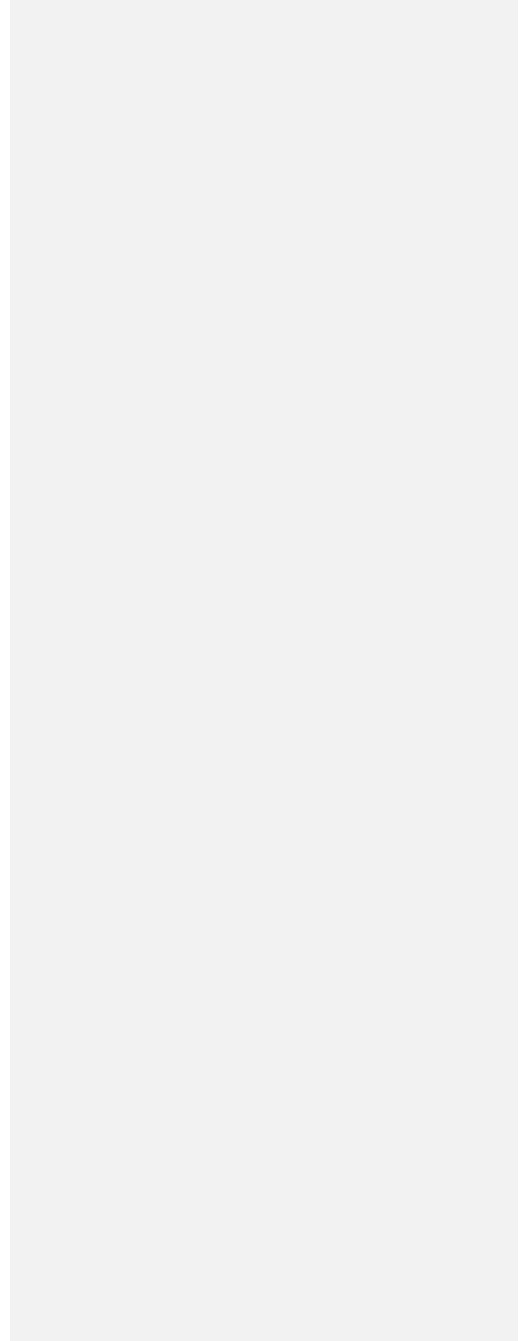


411 **Figure 3.** Time series of water levels, wind speed, and precipitation within the study area. (A) Computed water levels at various
412 locations (blue for Beira, red for Buzi village, and green for upstream in the Pungwe estuary (see Figure 2C for their location)
413 and the black dashed line representing the astronomical prediction at Beira. (B) Simulated wind speed (blue) and rainfall rate (red)
414 over the same period. Idai made landfall on March 15, and its powerful winds and rainfall resulted in marine flooding at Beira and
415 riverine-driven flooding upstream in the estuary. The vertical line represents the moment of landfall.
416

417 Validation of the SFINCS model for the observed extent (blue colors in [Figure 4](#)Figure 4A) gives confidence in the ability to
 418 simulate the compound flooding ([Figure 4](#)Figure 4). The model can reproduce the Sentinel-1 derived extent with a Critical
 419 Success Index of 0.59. This skill score is comparable to previous work by Eilander et al. (2022), albeit somewhat lower. Based
 420 on the differences between the modeled and satellite-derived extent, it becomes apparent that the model underestimates the
 421 flooding around the Buzi River (false negative; orange colors in [Figure 4](#)Figure 4B around 660-7800 km). We hypothesize
 422 this is due to the lack of river inflow related to an underestimation of rainfall further upstream and/or overestimation of
 423 infiltration due to soil saturation which is not considered. Moreover, the comparison with satellite-derived flood extent
 424 indicates an overestimation of the flooding at Beira (false positive; red colors in [Figure 4](#)Figure 4). Here, we suspect that the
 425 benchmark data might be off, and the coastal flooding already receded before the Sentinel data recorded the extent. The
 426 observed high-water marks near Beira ranged from 3.6 m within the estuary to 2.9 m \pm MSL at the open coast and are
 427 reproduced by SFINCS with respectively 3.8 and 3 m \pm MSL. This difference suggests a positive bias of the model results at
 428 the coast of \sim 10-20 cm, similar to the tidal validation (see Appendix 8.1), which revealed a median MAE of 21 cm.



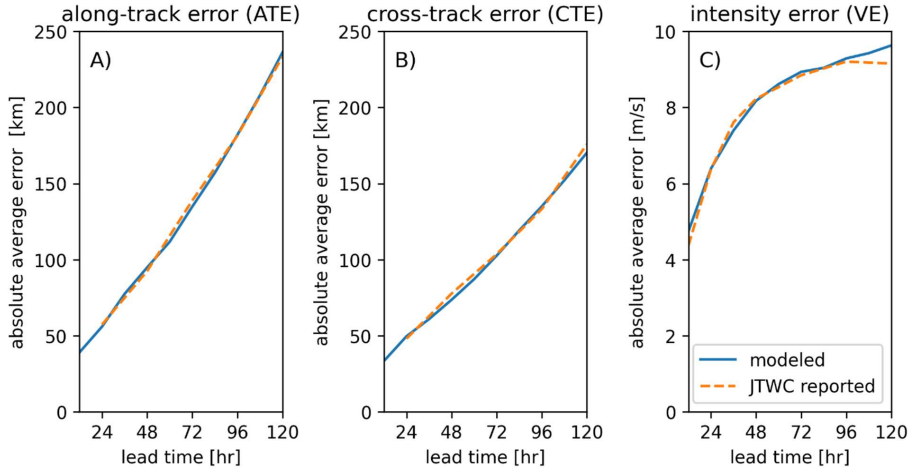
429 **Figure 4. Maximum computed water depth (Panel A) and binary skill of flood extents for Idai (Panel B).** Water depths are
 430 downscaled from the model resolution to the 10x10 meter resolution of the topo-bathymetry. The binary skill evaluation (Panel B)
 431 assists in determining the model's accuracy and dependability, and the Sentinel-1 radar data is used as a reference to determine
 432 skill. A true-positive (T-P) outcome denotes a correct flood prediction by the model compared to Sentinel-1 derived extent, whereas
 433 a false-positive (F-P) occurs when the model forecasts a non-existent flood. In contrast, a false-negative (F-N) indicates where
 434 the model overlooks an actual flood, and a true-negative (T-N) result occurs when the model accurately predicts the lack of a flood event.
 435 The model produces large-scale flooding, which is largely also observed in the data, but local differences of over- and
 436 underestimation exist. The coordinate system of this figure is WGS 84 / UTM 36 S (EPSG 32736). © Microsoft.



439 **5.2 Calibration and influence of simplifications of TC-FF**

440 **5.2.1 Calibration of TC-FF: mean absolute error and auto-regression**

441 This study used JTWC-reported errors for the along-track, cross-track, and intensity for the Southern Hemisphere to calibrate
442 our methodology (JTWC, 2021). For other case studies, for example, based on different forecasting agencies or in other ocean
443 basins), these reported errors can be used instead. Calibration is performed by minimizing the square-root difference between
444 computed and reported mean absolute values for various lead times using the Nelder-Mead method. This effort resulted in
445 mean absolute errors for B and D of 68.5 and 55.3 km and autoregression coefficients a_t , c_t , of 1.214 and 1.181 (Figure 5
446 5A and B) for the along-track and cross-track. Moreover, we calibrated the mean absolute error and regression coefficients for
447 the intensity, which resulted in mean absolute errors for F of 9.28 m/s and autoregression coefficient e_t of 0.624 (Figure 5C).

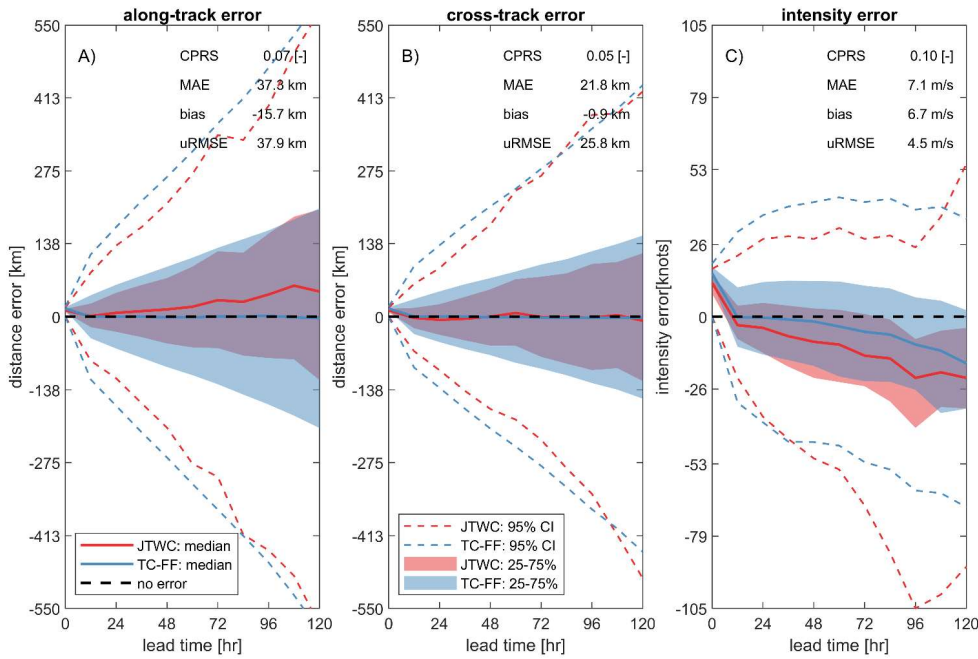


448
449 **Figure 5. Comparison of calibration results for the probabilistic forecasting method TC-FF (solid blue line) and the Joint Typhoon**
450 **Warning Center (JTWC) reported error statistics based on the 5-year average (2016-2020) in the Southern Hemisphere (dashed**
451 **orange line). Panel A represents the along-track error, Panel B demonstrates the cross-track error, and Panel C exhibits the wind**
452 **speed or intensity error. Modeled errors are based on 1,000 ensemble members. Modeled absolute average errors are similar to**
453 **JTWC.**

454 **5.2.2 Comparison of TC-FF with operational forecast products**

455 Errors produced by TC-FF are compared to the implementation from NOAA, NHC and JTWC that are used operationally.
456 Minor differences between the TC-FF and full implementation based on DeMaria et al. (2009) and De Maria et al. (2013) exist
457 and are attributed to the simplifications used in the error distribution (including the lack of GPCE) and lack of bias conditions.
458 The distribution in along-track, cross-track, and intensity error is typically in the same order (Figure 6), which is

459 confirmed by a median CPRS over various lead times from 0 to 120 hours of 0.07, 0.05, 0.10 and median MAE of 37 km, 21
460 km, and 7 m/s of for respectively the along-track, cross-track, and intensity. At the same time, TC-FF has by design no bias
461 corrections [in terms of cross-track, along-track and intensity errors](#), whereas the operational system does, leading to the positive
462 median along-track error in red compared to the blue line in [Figure 6](#)[Figure-6A](#) and a median bias of -16 km. Besides the
463 median estimates, the interquartile range (25-75%) and 95% CI- match relatively well for the along-track and cross-track errors.
464 Larger differences are found for the intensity error. In general, the wind intensity error looks visually erratic and doesn't start
465 at zero for no lead time, which is the result of the inland wind decay model. Both JTWC and TC-FF have a negative bias due
466 to the effect of land, but TC-FF does have a median bias of +6.7 m/s compared to JTWC, suggesting that TC-FF overestimates.
467 However, more substantial differences are found for the interquartile range and 95% CI. These findings for the along-track,
468 cross-track, and intensity are supported by a more detailed analysis of the CDF for the different parameters as a function of
469 lead time ([Figure 12](#)[Figure-12](#), [Figure 13](#)[Figure-13](#), [Figure 14](#)[Figure-14](#)). For the along-track and cross-track, we observe an
470 increase in the MAE and uRMSE as a function of lead time but a decrease in the CPRS. The increasingly larger error
471 distribution influences this pattern. Moreover, TC-FF produces Gaussian-distributed errors while the JTWC error distribution
472 differs since it is based on historical error distribution and adjusted based on the GPCE. Similar to [Figure 6](#)[Figure-6](#), larger
473 differences are found for the intensity error, which is influenced by the bias correction that increases with lead times.



474
 475 **Figure 6.** Comparison of validation results for the probabilistic forecasting method TC-FF (blue line) and the Joint Typhoon
 476 Warning Center (JTWC) operational product (red line). Panel A represents the along-track error, Panel B demonstrates the cross-
 477 track error, and Panel C exhibits the wind speed or intensity error. Errors are computation for both the TC-FF and JTWC are
 478 based on 1,000 ensemble members. Solid lines are median estimats, shaded areas the interquantile range (25-75% CI) and dashed
 479 line the 95% CI. TC-FF and JTWC produce broadly similar error distributions for different lead times.

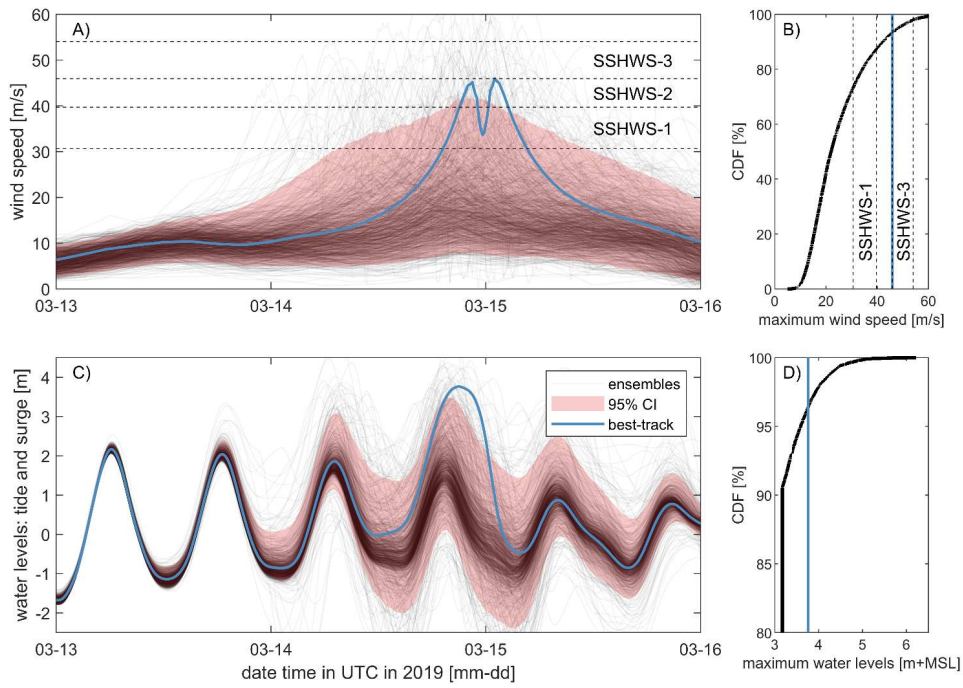
480 5.3 Forecasting of Idai using the TC-FF

481 This section presents the application of forecasting Idai using the TC-FF.

482 5.3.1 Uncertainty three days before landfall

483 The TC-FF method with 10,000 ensemble members is applied to the case of Cyclone Idai. The results reveal that accounting
 484 for the uncertainty of the TC track and intensity of eye three days before landfall results in considerable uncertainty regarding
 485 wind speeds and water levels near Beira (Figure 7Figure-7) or the region (Figure 8Figure-8). In particular, the wind speeds
 486 show a 95% CI of about 7-40 m/s at the moment of landfall (Figure 7Figure-7A) versus ~45 m/s or a Saffir-Simpson Hurricane
 487 Wind Scale (SSHWS) of 2 of the best track. Moreover, TC category 1 wind speeds could occur as early as March 15⁴ at

488 0724:30 UTC or as late as March 16-15 at 1911:50-10 UTC. This spread of possible maximum wind speeds at Beira results
489 from the large uncertainties in intensity and a difference in landfall location and time. Based on the same model simulations,
490 the empirical cumulative distribution function (CDF) of the maximum wind speed at Beira ranges from 8.8 to 59.2 with a
491 median wind speed of 25.5 m/s, while the best track has a 5.9% exceedance probability (Figure 7Figure-7B). Consequently,
492 water levels vary greatly (Figure 7Figure-7C). For example, ensemble members can exhibit a sizeable wind-driven setup due
493 to TC wind blowing from offshore into the estuary, pushing water up in the estuary and at Beira. For landfall locations west
494 of the estuary, the wind blows offshore, resulting in a large set-down. Note that Beira is in the Southern Hemisphere, and due
495 to the Coriolis effect, TCs spin clockwise. The highest water levels occur when high tide and wind-driven setup coincide,
496 which explains the three peaks in the 95% CI water level given the semi-diurnal tide and the highest possible wind speed for
497 ~1.5 days (Figure 7Figure-7C). The maximum water levels are dominated by the tide except in the situation of cyclone impact
498 (see the CDF in Figure 7Figure-7D and the minimum value of ~3.5m+MSL around 90%, which is influenced by the tide and
499 time window over which it is determined). The specific track of Idai resulted in relatively extreme conditions compared to
500 other possible combinations (both for winds and water levels). A similar pattern can be observed in the spatial maps shown in
501 Figure 8. The average probability of flooding in the area is 26%, with higher probabilities of flooding found in the lower-lying
502 portions of the estuary (note we are excluding points below MSL; Figure 8Figure-8A). The 1% exceedance flood depth
503 threshold shows a large extent and is quite similar to the computed extent due to Idai (see Figure 4Figure-4A for comparison
504 with Figure 8B). The main difference is that there is more flooding near the city of Beira and somewhat less near Buzi Village.
505 The match between the 1% exceedance flood depth and the best track with Idai suggests that the event was relatively severe
506 and implies that even though many other potential scenarios could have unfolded, they likely would not have resulted in the
507 same extensive flooding caused by Idai.



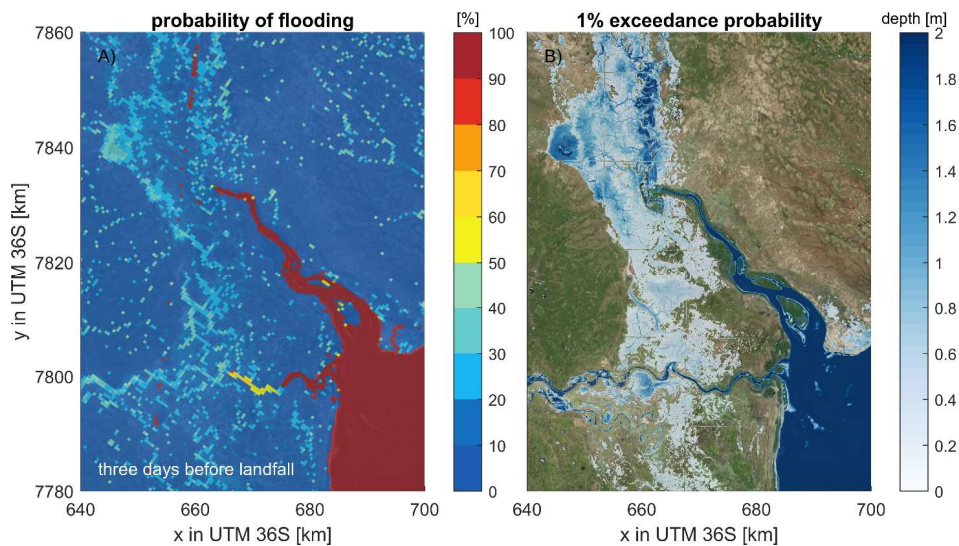
508

509 **Figure 7. Multi-panel Analysis of wind and water Levels three days before landfall: (A) time series of wind speeds, (B) maximum**
 510 **wind speeds, (C) time series of water levels near Beira, and (D) maximum water levels. Data is derived from 10,000 ensemble**
 511 **members (black transparent line; every 10th plotted) with red shading representing the 95% CI. The best track (blue line) and the**
 512 **Saffir-Simpson Hurricane Wind Scale are included for comparison (panels A and B only). There is substantial uncertainty in wind**
 513 **speeds and water levels near Beira three days prior to landfall.**

514

515

516



517
518

519 **Figure 8. Probabilistic flood analysis for Cyclone Idai three days before landfall: (A) Spatial distribution of flooding probability; (B)**
 520 **Corresponding 1% exceedance water depth estimates, highlighting areas at most significant hazard. Results in panel A are**
 521 **determined from 10,000 ensemble members on the original 500-meter model resolution, while water depth in panel B is**
 522 **downscaled to the original 10x10-meter bathymetry resolution. Higher probabilities of flooding are found in the lower-lying portions of the**
 523 **estuary. The coordinate system of this figure is WGS 84 / UTM 36 S (EPSG 32736). © Microsoft.**

524 5.3.2 Influence of sampling size

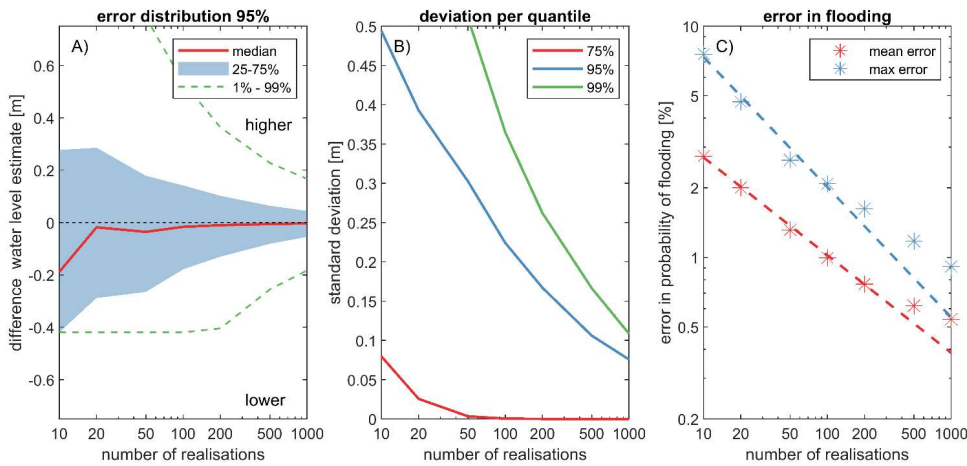
525 As described by Cashwell and Everett (1959) and DeMaria et al. (2009), the precision of Monte Carlo techniques is
 526 proportional to the number of ensemble members (N). The convergence rate typically shows a slower progression than 1/N,
 527 constituting a limitation intrinsic to all Monte Carlo methods. To investigate the convergence rate and the error induced by
 528 employing a finite number of ensemble members, the Idai forecasting case three days prior to landfall is used, analogous to
 529 the preceding section, albeit with a variable number of ensemble members. Additionally, bootstrapping is employed to
 530 approximate convergence rates and the accompanying uncertainty.

531

532 The estimation of the 95% exceedance maximum water levels in proximity to Beira exhibits convergence with the number of
 533 ensemble members, albeit with considerable deviations compared to a fully converged solution with 10,000 members when
 534 implementing a low number of ensemble members (Figure 9A). For instance, employing merely 50 ensemble members results
 535 in an interquartile range (25-75%) of -0.28 to +0.10 m. Increasing the number of ensemble members reduces this sampling
 536 uncertainty to a range of -0.09 to +0.06 m for 200 ensemble members.

537 Similarly, the standard deviation for several quantiles of maximum water level estimates at Beira reduces with more ensemble
 538 members. It exhibits a similar pattern from higher to lower quantiles (Figure 9B). In essence, estimating rare events necessitates
 539 executing more ensemble members to attain comparable convergence. This study found that the 95% exceedance maximum
 540 water level at Beira when utilizing 200 ensemble members has a standard deviation of 21 cm (blue line Figure 9B). This level
 541 of convergence seems acceptable since it is in a similar order as the skill of the hydrodynamic model (see Section 5.1).
 542

543 The probability of error in flood potential is expressed as a function of N on a log-log plot (Figure 9C). Compared to a fully
 544 converged solution with 10,000 members, for N=200, the mean error constitutes 0.95%, and the maximum error amounts to
 545 1.53%. Note that this estimate is without considering the model error. In the log-log diagram, the errors exhibit near-linear
 546 correlations with N and could serve as a basis for determining the number of ensemble members needed for a specified
 547 confidence level. For instance, to achieve a maximum error of 1% in flood probability, it would be necessary to utilize 500
 548 ensemble members.



549
 550 **Figure 9. Sampling size effects on flood estimation accuracy. (A) Quantiles of sampling error for the 5% exceedance water level. (B)**
 551 **Standard deviation of 75%, 95%, and 99% quantiles, illustrating the uncertainty in estimation. (C) Comparison of maximum and**
 552 **average error in flood probability predictions. All panels were generated using 10,000 ensemble members and a 1000-bootstrap**
 553 **resampling approach. Using more ensemble members reduces the sampling uncertainty.**

554 5.3.3 Importance of lead time

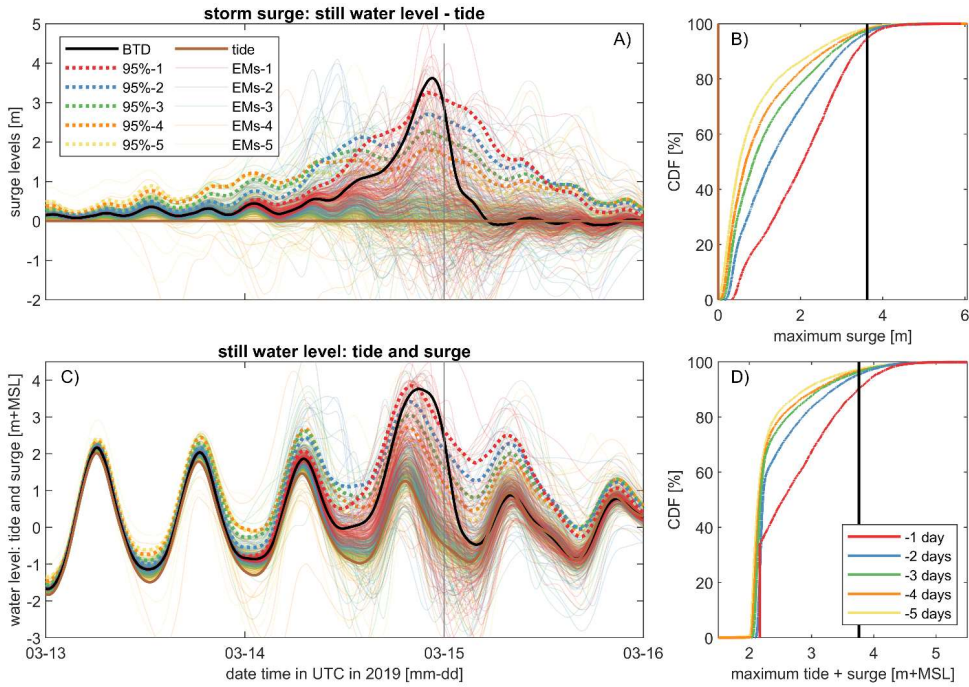
555 Thus far, the probabilistic TC forecasting framework has been implemented three days prior to the landfall of Idai.
 556 Nevertheless, the forecast's results fluctuate with lead times, consequently influencing the associated evaluations of water
 557 levels (Figure 10) and flood probabilities (Figure 11).

558

559 The predicted water levels (tide + surge) vary with lead times (Figure 10A and C). Specifically, at a lead time of
560 five days before landfall, an (unsurprisingly) larger spread between the ensemble members is observed compared to lead times
561 of, for example, one or three days. Moreover, as landfall approaches, the time series converges since increasing ensemble
562 members produce highly similar predictions. For example, notice how individual ensemble members 1 day before landfall
563 show similar storm surges and still water levels (i.e., the concentration of lines which becomes more apparent in Figure
564 10). Moreover, the 5% and 95% exceedance values become less spread out and more peaked around landfall (dashed
565 lines in Figure 10). This convergence is more apparent for the storm surge. The CDF of the maximum storm surge
566 levels increases with reducing lead time (Figure 10B). For example, the median storm surge increases from 0.5m
567 five days before landfall to 0.9 and 2.0m for lead times of three days and one day, respectively (notice the increasing median
568 estimate in the CDF plot from 5 to 1 day in Figure 10B). This increase in maximum storm surge shows the increasing
569 certainty that the TC will land near Beira. However, for other locations, the opposite may occur as the landfall shifts away
570 from it. The still water levels are influenced by both tidal motions and the influence of the TC (Figure 11C). This
571 strongly influences the maximum computed still water level (Figure 11D). For instance, the lowest maximum water
572 level for all simulations is around ~2 m above MSL, resulting from the maximum tidal range rather than the TC itself. The 95th
573 quantile of the maximum still water level is 3.4 m + MSL five days prior to landfall, which increases to 3.6 and 4.0 m+MSL
574 for lead times of three days and one day, respectively. The best track of Idai is included as a reference and estimated to have a
575 9% probability of exceedance 1 day before landfall.

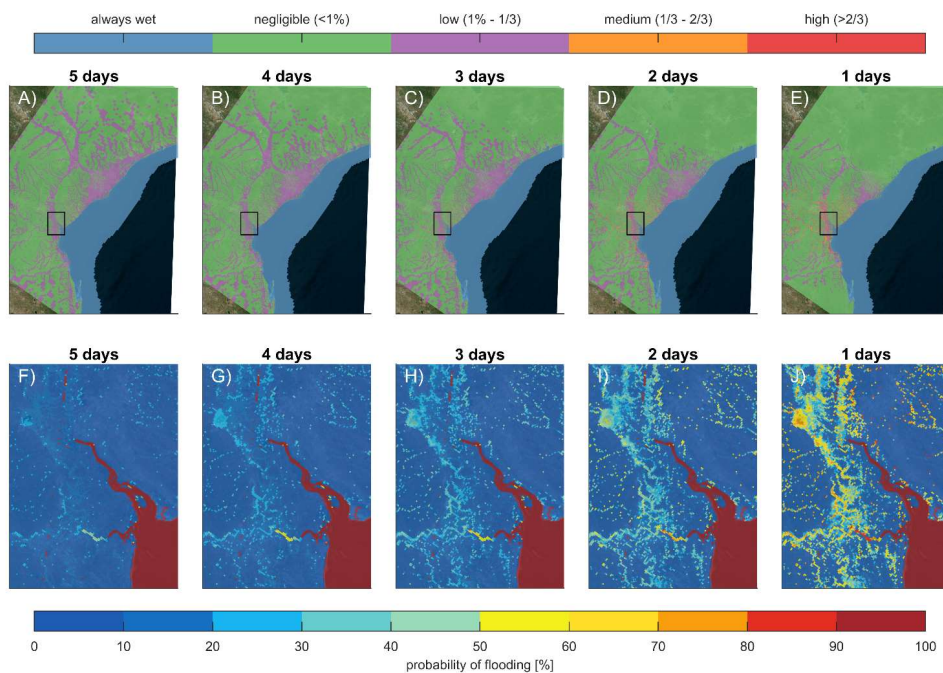
576

577 A large portion of the Sofala province faces a minor flood risk five days before the actual landfall. The flood probability for
578 the estuary near Beira increases as lead times reduce (Figure 11B). In particular, the average probability of flooding five days
579 before landfall is 15%, increasing to 17 and 24% for lead times of three and one day, respectively. Conversely, for the entire
580 model domain, a probability of greater than 1% flooding declines from 97 to 94 and 64 km² for lead times of five, three, and
581 one day (Figure 10A). In other words, five days before landfall, less confidence in predictions translates into more spatial
582 variability on flooding probability tied to a larger impact area. Closer to the actual landfall, there is more certainty over which
583 area will be affected.



584

585 **Figure 10. Forecasted water levels in Beira for 1-5 day lead times: temporal evaluation and cumulative distribution. Panel A and C:**
 586 **Time series illustrating the forecasted water levels in proximity to Beira with lead times ranging from 1 to 5 days prior to landfall**
 587 **showcasing both individual ensemble members (solid transparent lines; every 100th plotted), tide-only (brown), best-track (black)**
 588 **and quantile estimates (95% dashed lines). Panels A and C use the same colors and line styles. Panel B and D: Cumulative**
 589 **distribution function (CDF) showing the maximum water levels in ascending order for all ensemble members, providing insights**
 590 **into the probability of occurrence for various water level thresholds. Panels B and D use the same colors. Panels A and B show the**
 591 **storm surge levels (computed still water levels minus predicted tidal levels), while Panels C and D present the still water level (tide**
 592 **and surge).**



593

594 **Figure 11. Evolution of the flood probability prior to landfall: Panels A-E depict the spatial distribution of flooding probabilities at**
 595 **5, 4, 3, 2, and 1 day(s) before landfall, respectively. Color gradients represent the varying probability. The top panels focus on the**
 596 **entire area simulated and the bottom panels on the Pungwe and Buzi river deltas. With decreasing lead time, the area that could be**
 597 **affected decreases while there is an increased probability of flooding near Beira. The coordinate system of this figure is WGS 84 /**
 598 **UTM 36 S (EPSG 32736). © Microsoft.**

599

600 6 Discussion

601 This paper describes a new probabilistic method to forecast TC-induced coastal compound flooding by tide, surge, and rainfall
602 using Monte Carlo sampling. Due to the limited number of observations on TC evolution, for short-term operational analyses,
603 an autoregressive technique that imposes potential errors on top of the forecasted track is preferred over those parametric
604 sampling techniques used for long-term ~~and~~ strategic risk assessments based on historical records (e.g., Nederhoff et al., 2021).
605 In addition, for the same scarcity of observation, there is limited knowledge of the underlying joint distribution between TC
606 and ocean characteristics, which makes Monte Carlo sampling preferred compared to sampling techniques that are highly
607 efficient for complex multivariate patterns such as cluster analysis (e.g., Choi et al., 2009) and MDA methods (e.g., Bakker et
608 al., 2022). However, exploring the possibility of increasing efficiency via the aforementioned methods is important, especially
609 since the error space increases as a function of lead time, and estimating these events requires increasing amounts of ensemble
610 members (Figure 9B). However, this is a topic that requires an in-depth analysis and is beyond the scope of the present study.

611
612 Compared to the implementation of DeMaria et al. (2009) and DeMaria et al. (2013), the ensemble generation is simplified by
613 removing bias corrections, applying a single normal error distribution calibrated on historical errors (Figure 5Figure-5), and
614 does not account for the uncertainty of the track forecasts on a case-by-case basis via GPCE. While we acknowledge these
615 simplifications, this method does make it possible to account for TC forecasting errors for any ocean basin based on reported
616 average historical errors alone. Nevertheless, the behavior of a specific tropical cyclone (TC) does not necessarily conform to
617 the "average" pattern, and differences between the operational JTWC model were found (Figure 6Figure-6). For Beira, we
618 found minor differences in the comparison of TC-FF and JTWC operational ensembles that do account for the uncertainty of
619 the track forecasts on a case-by-case basis. Thus the case study presented in this paper, suggests that the universal historical
620 error statistics versus a TC-dependent error sampling might be acceptable, however, follow-up work will be needed to test if
621 this findings holds for other TCs. Moreover, the system only accounts for uncertainty in track parameters and does not account
622 for uncertainty in, for example, rainfall or computed storm surge. The implications of these assumptions on the precision and
623 predictive proficiency of our approach for coastal compound flooding remain undetermined. Our implementation has been
624 recently integrated into an operational system tailored for the contiguous United States. Verification of the reliability of this
625 operational system is currently pending. Regardless, TC-FF compares well with the predictions provided by ECMWF of Idai
626 that showed a probability of 50 to 90% of severe flooding four to one day before landfall (Figure 10Figure-10). We hypothesize
627 that track uncertainties dominate several days before landfall while <1-day other sources of uncertainty start to become more
628 important and should ideally be accounted for.

629
630 In the introduced methodology, we apply the compound flooding model SFINCS. ~~While-†~~The validation gave confidence that
631 the hydrodynamic model reproduces the main tidal motions and flooding during Idai.; ~~D~~differences did exist compared to the
632 (limited) validation data (Figure 4Figure-4). Additional data sources to assess the model's spatiotemporal accuracy and

633 [reliability in simulating the compound flooding event would be advantageous but were unavailable \(at the time this study was](#)
634 [performed\)](#). The model skill could be improved by including additional wind radii information in the parametric wind model
635 (e.g. radius of gale force winds along different quadrants) and more accurately resolving on-land winds, rainfall, and infiltration
636 processes. For example, Done et al. (2020) present a methodology to account for terrain effects by adjusting winds from a
637 parametric wind field model by using a numerical boundary layer model. Here, we applied the IPET empirical relationship
638 that relates pressure drop to rainfall intensity. [We chose IPET over other methods since this relatively simple method](#)
639 [demonstrated the highest skill at reproducing storm-total precipitation in Brackins & Kalyanapu \(2020\)](#). However, [Initially,](#)
640 [deployment showed the necessity to triple the rainfall rate due to severe underestimation of the total rainfall and associated](#)
641 [flooding. We hypothesize this does influence model skill from SFINCS but suspect limited influence in results geared towards](#)
642 [TC-FF applicability and sensitivity regarding sample size and lead time.](#) Improvement (deterministic or stochastic
643 parametrizations) of TC rainfall could overcome this limitation. [For example, we acknowledge that there are other](#)
644 [computationally efficient TC rain models in the literature that might perform better \(e.g., Lu et al. 2018\) and are exploring](#)
645 [incorporating these methods in TC-FF.](#) Moreover, SFINCS was run with a constant infiltration rate and does not account for
646 drainage systems, [fluvial discharge from the large catchment](#) and flood protection measures besides the frontal levee. It is also
647 unknown how the topo-bathymetry that was collected before Idai influenced results. Lastly, the effects of waves (e.g., setup,
648 runup, overtopping) and morphological change were not considered. All these limitations affect the model skill and could
649 explain some mismatches observed compared to Sentinel-1 data and high-water marks at Beira. However, the computational
650 efficiency of SFINCS allowed us to run thousands of ensemble members on limited computational resources. We accept the
651 loss of some model accuracy with this gain of speed. [For future developments, we do envision accounting for these](#)
652 [uncertainties in addition to variability in track parameters.](#)

653
654 The focus of the development of TC-FF has been geared to the computation of overland flooding. However, TCs pose
655 significant hazards through both water *and* wind. A study by Rappaport (2014) indicated that from 1963 to 2012 in the United
656 States, approximately 90% of fatalities associated with tropical cyclones were due to water-related incidents. The wind-related
657 fatalities were about 8%. This does not provide insight into the cause of damage associated with landfalling TCs, nor does it
658 provide insight into how these ratios vary across the globe. Regardless, TC-FF does provide the possibility to estimate extreme
659 wind speeds and link this to potential damage as an additional data product. Including wind damage as part of our framework
660 is something we are planning to work on in the future. [Moreover, while this study was written from an operational short-term](#)
661 [risk analysis perspective, the same methodology can also be used within strategic long-term risk analysis to explore](#)
662 [perturbations to the track and perform ‘what if’ sensitivity testing to coastal flooding \(see e.g., Rye and Boyd 2022\).](#)

663 **7 Conclusions**

664 A new method and highly flexible open-source tool was developed to perform probabilistic forecasting of tropical cyclone-
665 induced coastal compound flooding. The Tropical Cyclone Forecasting Framework, TC-FF, computes a set of ensemble
666 members based on a simplified DeMaria et al. (2009) method. In particular, TC-FF uses gridded time- and spatially-varying
667 wind and pressure fields or forecasted tracks and combines this with historical observed error on the along-track, cross-track,
668 and intensity. Subsequently, the tool creates a temporally and spatially varying wind field, including rainfall, to force a
669 computationally efficient compound flood model. This approach allows for the inference of probabilistic wind and flood hazard
670 maps calibrated to any ocean basin in the world with limited computational resources. In contrast to the current practice, TC-
671 FF allows uncertainty analysis using large ensembles produced with physics-based models, narrowing down confidence bands
672 on forecasting coastal compound flooding focused on operational TC risk analyses.

673

674 The validation of the quadtree SFINCS model for Mozambique's Sofala province showed reliable skill in terms of tidal
675 propagation in the area of interest (median MAE of 21 cm), including good skill in reproducing the observed flood extent for
676 the case of the flooding caused by Cyclone Idai (2021). The model was able to reproduce the storm surge generation during
677 landfall and flooding near the city of Beira, including the subsequent compound flooding resulting from rainfall runoff in the
678 Pungwe estuary (critical success index of 0.59). Moreover, the model runs efficiently with a wall clock time of 4 minutes for
679 a 7-day event allowing it to be deployed in probabilistic operational assessments when using multiple cores.

680

681 TC-FF was calibrated with the average reported errors for the southern hemisphere via the Nelder-Mead method to determine
682 the mean absolute errors and autoregression coefficients. A comparison between TC-FF and JTWC (based on the complete
683 implementation of DeMaria et al., 2009) and DeMaria et al., 2013) revealed minor differences. In particular, for various lead
684 times from 0 to 120 hours, a median Continuous Ranked Probability Score (CRPS) of 0.07, 0.05, 0.10 and median MAE of 37
685 km, 21 km, and 7 m/s for respectively the along-track, cross-track, and intensity error were found. These findings give
686 confidence that the TC-FF, including the simplified DeMaria et al. (2009) implementation, can be used for more generalized
687 applications in data-scarce environments.

688

689 TC-FF provides valuable insights into the uncertainty of wind speeds, water levels, and potential flooding due to Idai, revealing
690 the impacts of track and intensity uncertainties. This is demonstrated in the wide array of possible maximum wind speeds and
691 significant fluctuations in water levels, which are primarily affected by tidal influences and the cyclone. For instance, even
692 just three days prior to landfall, there's a broad spread in the predicted flood areas. This suggests that there is still a significant
693 chance that Idai may not hit the anticipated area or may not generate a substantial storm surge.

694

695 The precision of forecasts is directly related to the number of ensemble members used. A mean error in flood probability of
696 less than 1% and <20 cm sampling errors for the 1% exceedance water level at Beira required 200 members. Based on that,
697 we determine that at least 200 ensemble members are needed to get reliable water levels and flood results three days before
698 landfall. A higher number of ensemble members reduces sampling uncertainty and increases the accuracy of water level and
699 flood potential estimates.

700

701 The lead time before landfall has a considerable impact on the forecast's precision. As the lead time decreases, the variability
702 of forecasts diminishes, and the forecasts converge to similar predictions. Similarly, the probability of flooding in certain areas,
703 such as the estuary near Beira, increases as the lead time shortens, providing more certainty over the areas that will be affected
704 by the event.

705

706 TC-FF offers a significant advancement compared to the current status quo of a single deterministic simulation when
707 forecasting tropical cyclone compound flooding hazards. This approach facilitates a comprehensive understanding of complex
708 interdependencies and uncertainties. By quantifying the likelihood of various outcomes (e.g. by estimating the probability of
709 major flooding in a given neighborhood days before landfall), probabilistic methods enable stakeholders to make more
710 informed decisions, allocate resources better, and enhance preparedness and resilience in the face of these catastrophic natural
711 phenomena.

712

713 *Code and data availability.*

714 ~~The code and data are freely available to other researchers and consultants.~~ The Python code for this method [is freely available](https://doi.org/10.5281/zenodo.10433070)
715 [to anyone and publishedis accessible on Zenodo](https://doi.org/10.5281/zenodo.10433070) (<https://doi.org/10.5281/zenodo.10433070>)
716 [and GitHub](https://github.com/Deltares-research/cht_cyclones) (https://github.com/Deltares-research/cht_cyclones).
717 ~~<https://github.com/Deltares/CoastalHazardsToolkit>.~~

718

719 *Author contributions.*

720 KN and MvO developed the method and the outline for the manuscript. KN wrote the initial manuscript, with editorial
721 comments by JV, AvD, JA, TL and DR.

722

723 *Competing interests.*

724 The authors declare that they have no conflict of interest.

725

726 *Acknowledgments and financial support*

727 The authors thank the Deltares research programs 'Natural Hazards' and 'Risk Analysis and Management', which have provided
728 financing to develop and write this paper. Moreover, we want to thank Buck Sampson for input and data regarding the
729 operational wind field probabilities. [The authors also would like to thank two anonymous reviewers for their comments and](#)
730 [help in improving this paper](#)
731

732 **8 Appendices**

733 **8.1 Tidal calibration and validation**

734 A tidal calibration was performed on the SFINCS computed tidal constituents compared to the tidal constituents at Beira.
 735 Constituents with an amplitude of more than 5 cm (M2, S2, N2, K2, and K1) were adjusted in terms of amplitude
 736 (multiplication) and phase (addition). Amplitude changes varied between 0.84 and 1.07 while phase difference changed on
 737 average by 40°. These calibration steps of adjusting the tidal constituents substantially reduced tidal errors at the Beira from a
 738 MAE of 43 to 17 cm. Secondly, model skill in reproducing tidal amplitudes and phases is assessed at 7 tide stations across the
 739 area of interest (including the calibration station of Beira). The SFINCS model reproduces tide with a median MAE of 21 cm,
 740 median RMSE of 25 cm, and median difference in M2 and S2 amplitude and phase of respectively -10 and -1 cm and -10 to -
 741 12° (median values computed over the different stations). Our hypothesis is that the reduction in tidal error observed at Beira
 742 throughout the calibration process might be due to a misalignment in the amplitudes and phases of the TPXO model which
 743 were used to generate the tidal boundary conditions (see Section 3.1.2). Presumably, the bathymetry contributes to the error
 744 observed in the validation process.

745

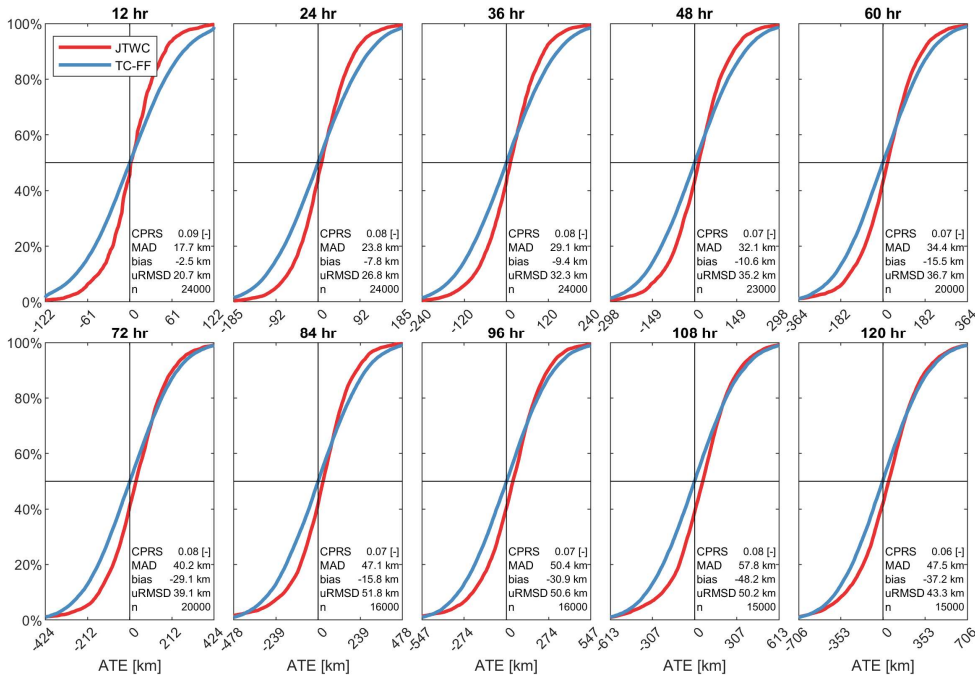
746 **Table A1. Evaluation of model proficiency in replicating tides near the Sofala province. Stations are ordered south to north. Columns**
 747 **one and two present the Mean Absolute Error (MAE) and Root Mean Square Error (RMSE), respectively, as error metrics for the**
 748 **comparison between observed and simulated tidal time series. The final four columns display the discrepancy (Δ) in amplitude (Δ)**
 749 **and phase difference (ϕ) for the two most prominent tidal constituents in the area (M2 and S2), where Δ is calculated as the difference**
 750 **between observed and simulated values.**

Name	MAE [m]	RMSE [m]	Δ M2 A [m]	Δ M2 ϕ [°]	Δ S2 A [m]	Δ S2 ϕ [°]
Bazaruto	0.13	0.15	-0.10	-7	0.01	-2
Bartolomeu Dias	0.12	0.15	-0.14	1	-0.11	-1
Chiloane	0.30	0.41	0.20	-10	0.08	-15
Beira	0.17	0.20	0.00	0	0.00	0
Chinde	0.21	0.25	-0.08	-13	-0.01	-12
Quelimane	0.26	0.32	-0.14	-15	-0.09	-21
Pebane	0.21	0.25	-0.14	-11	-0.09	-15
Median	0.21	0.25	-0.10	-10	-0.01	-12

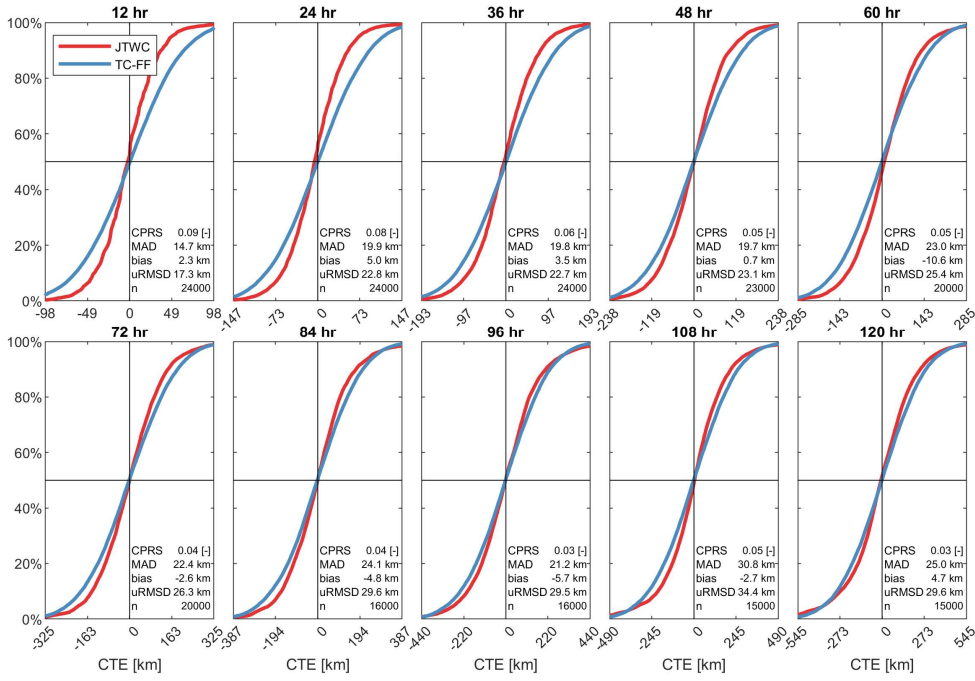
751

752 **8.2 Additional figures for Section 5.2.2. 'Influence of simplification in TC-FF'**

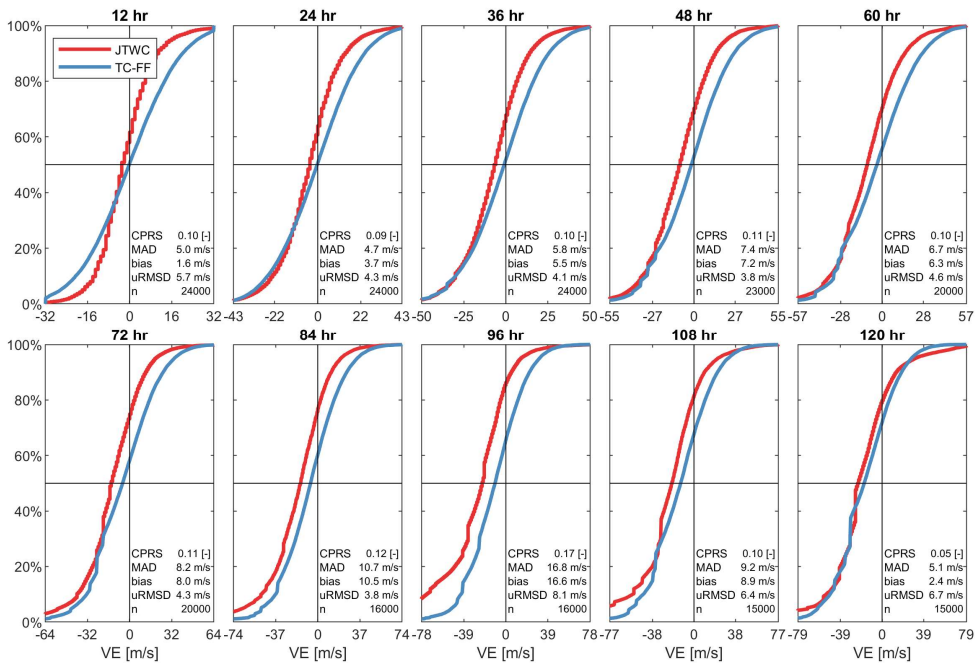
753 [Figure 12](#), [Figure 13](#) and [Figure 14](#) provide additional information for Section 5.2.2. 'Influence
754 of simplification in TC-FF'.



755
756 **Figure 12. Comparison between the cumulative distribution function (CDF) of the along-track-error (ATE) for JTWC (red;**
757 **reference) and TC-FF (blue; modeled). The different panels represent different lead times.**



758
 759 **Figure 13. Comparison between the cumulative distribution function (CDF) of the cross-track-error (CTE) for JTWC (red;**
 760 **reference) and TC-FF (blue; modeled). The different panels represent different lead times.**



761
 762 **Figure 14. Comparison between the cumulative distribution function (CDF) of the intensity error (VE) for JTWC (red; reference)**
 763 **and TC-FF (blue; modeled). The different panels represent different lead times.**

764

765

766 **9 References**

- 767 Agriculture, U. S. D. of. (2009). *National Engineering Handbook Chapter 7 Hydrologic Soil Groups*.
- 768 Alfieri, L., Burek, P., Dutra, E., Krzeminski, B., Muraro, D., Thielen, J., & Pappenberger, F. (2013).
769 GloFAS-global ensemble streamflow forecasting and flood early warning. *Hydrology and Earth*
770 *System Sciences*, 17(3), 1161–1175. <https://doi.org/10.5194/hess-17-1161-2013>
- 771 Ayyad, M., Orton, P. M., El Safty, H., Chen, Z., & Hajj, M. R. (2022). Ensemble forecast for storm tide
772 and resurgence from Tropical Cyclone Isaias. *Weather and Climate Extremes*, 38(May), 100504.
773 <https://doi.org/10.1016/j.wace.2022.100504>
- 774 Bakker, T. M., Antolínez, J. A. A., Leijnse, T. W. B., Pearson, S. G., & Giardino, A. (2022). Estimating
775 tropical cyclone-induced wind, waves, and surge: A general methodology based on representative
776 tracks. *Coastal Engineering*, 176(August 2021). <https://doi.org/10.1016/j.coastaleng.2022.104154>
- 777 [Brackins, J. T., & Kalyanapu, A. J. \(2020\). Evaluation of parametric precipitation models in](https://doi.org/10.1016/j.jhydrol.2019.124255)
778 [reproducing tropical cyclone rainfall patterns. *Journal of Hydrology*, 580.](https://doi.org/10.1016/j.jhydrol.2019.124255)
779 <https://doi.org/10.1016/j.jhydrol.2019.124255>
- 780 Chen, B. F., Kuo, Y. Te, & Huang, T. S. (2023). A deep learning ensemble approach for predicting
781 tropical cyclone rapid intensification. *Atmospheric Science Letters*, 24(5), 1–11.
782 <https://doi.org/10.1002/asl.1151>
- 783 Choi, K.-S., Kim, B.-J., Choi, C.-Y., & Nam, J.-C. (2009). Cluster analysis of Tropical Cyclones
784 making landfall on the Korean Peninsula. *Advances in Atmospheric Sciences*, 26(2), 202–210.
785 <https://doi.org/10.1007/s00376-009-0202-1>
- 786 de Vries, H. (2009). Probability Forecasts for Water Levels at the Coast of The Netherlands. *Marine*
787 *Geodesy*, 32(2), 100–107. <https://doi.org/10.1080/01490410902869185>
- 788 Deltares. (2021). *Beira Coastal Protection Preparation study : flood hazard modelling*.
- 789 Deltares. (2018). *Wind Enhance Scheme for cyclone modelling - User Manual*. 1–110.
- 790 DeMaria, M., Knaff, J. A., Brennan, M. J., Brown, D., Knabb, R. D., DeMaria, R. T., Schumacher, A.,
791 Lauer, C. A., Roberts, D. P., Sampson, C. R., Santos, P., Sharp, D., & Winters, K. A. (2013).

- 792 Improvements to the operational tropical cyclone wind speed probability model. *Weather and*
793 *Forecasting*, 28(3), 586–602. <https://doi.org/10.1175/WAF-D-12-00116.1>
- 794 DeMaria, M., Knaff, J., Knabb, R., Lauer, C., Sampson, C., & DeMaria, R. T. (2009). A New Method
795 for Estimating Tropical Cyclone Wind Speed Probabilities. *Weather and Forecasting*, 24(6),
796 1573–1591. <https://doi.org/10.1175/2009WAF2222286.1>
- 797 [Done, J. M., Ge, M., J. Holland, G., Dima-West, I., Phibbs, S., R. Saville, G., & Wang, Y. \(2020\).](#)
798 [Modelling global tropical cyclone wind footprints. *Natural Hazards and Earth System Sciences*,](#)
799 [20\(2\), 567–580. <https://doi.org/10.5194/nhess-20-567-2020>](#)
- 800 Doyle, J., Hodur, R., Chen, S., Jin, Y., Msokaitis, J., Wang, S., Hendricks, E., Jin, J., & Smith, T.
801 (2014). Tropical Cyclone Prediction Using COAMPS-TC. *Oceanography*, 27(3), 104–115.
802 <https://doi.org/10.5670/oceanog.2014.72>
- 803 [Easterling, D. R., Meehl, G. A., Parmesan, C., Changnon, S. A., Karl, T. R., & Mearns, L. O. \(2000\).](#)
804 [Climate extremes: observations, modeling, and impacts. *Science \(New York, N.Y.\)*, 289\(5487\),](#)
805 [2068–2074. <https://doi.org/10.1126/science.289.5487.2068>](#)
- 806
- 807 Egbert, G. D., & Erofeeva, S. Y. (2002). Efficient inverse modeling of barotropic ocean tides. *Journal*
808 *of Atmospheric and Oceanic Technology*, 19(2), 183–204. [https://doi.org/10.1175/1520-0426\(2002\)019<0183:EIMOBO>2.0.CO;2](https://doi.org/10.1175/1520-0426(2002)019<0183:EIMOBO>2.0.CO;2)
- 810 Eilander, D., Couasnon, A., Leijnse, T., Ikeuchi, H., Yamazaki, D., Muis, S., Dullaart, J., Winsemius,
811 H. C., & Ward, P. J. (2022). A globally-applicable framework for compound flood hazard
812 modeling. *EGUsphere*, 2022(April), 1–40. <https://doi.org/10.5194/egusphere-2022-149>
- 813 Emerton, R., Cloke, H., Ficchi, A., Hawker, L., de Wit, S., Speight, L., Prudhomme, C., Rundell, P.,
814 West, R., Neal, J., Cuna, J., Harrigan, S., Titley, H., Magnusson, L., Pappenberger, F., Klingaman,
815 N., & Stephens, E. (2020). Emergency flood bulletins for Cyclones Idai and Kenneth: A critical
816 evaluation of the use of global flood forecasts for international humanitarian preparedness and
817 response. *International Journal of Disaster Risk Reduction*, 50, 101811.
818 <https://doi.org/10.1016/j.ijdr.2020.101811>
- 819 Flowerdew, J., Horsburgh, K., Wilson, C., & Mylne, K. (2010). Development and evaluation of an
820 ensemble forecasting system for coastal storm surges. *Quarterly Journal of the Royal*
821 *Meteorological Society*, 136(651), 1444–1456. <https://doi.org/10.1002/qj.648>

Formatted: Swedish (Sweden)

- 822 [Fossell, K. R., Ahijevych, D., Morss, R. E., Snyder, C., & Davis, C. \(2017\). The practical predictability](#)
823 [of storm tide from tropical cyclones in the gulf of Mexico. *Monthly Weather Review*, 145\(12\),](#)
824 [5103–5121. *https://doi.org/10.1175/MWR-D-17-0051.1*](#)
- 825 Goerss, J. S. (2007). Prediction of consensus tropical cyclone track forecast error. *Monthly Weather*
826 *Review*, 135(5), 1985–1993. <https://doi.org/10.1175/MWR3390.1>
- 827 Gonzalez, T., & Taylor, A. (2018). *Development of the NWS' Probabilistic Tropical Storm Surge*
828 *Model*. 2018.
- 829 [Harper, B. A., Kepert, J. D., & Ginger, J. D. \(2010\). Guidelines for converting between various wind](#)
830 [averaging periods in tropical cyclone conditions. World Meteorological Organization, October.](#)
831 https://www.wmo.int/pages/prog/www/tcp/documents/WMO_TD_1555_en.pdf
- 832 Hasegawa, H., Kohno, N., & Itoh, M. (2015). Development of Storm Surge Model in Japan
833 Meteorological Agency. *14th International Workshop on Wave Hindcasting and Forecasting &*
834 *5th Coastal Hazard Symposium, May 2010*, 1–6.
- 835 Higaki, M., Hayashibara, H., & Nozaki, F. (2009). Outline of the High Resolution Global Model at the
836 Japan Meteorological Agency. *RSMC Tokyo-Typhoon Center Technical Review*, 11:25–38, 2009.
- 837 Holland, G. J., Belanger, J. ., & Fritz, A. (2010). A Revised Model for Radial Profiles of Hurricane
838 Winds. *American Meteorological Society*, 4393–4401. <https://doi.org/10.1175/2010MWR3317.1>
- 839 Hu, K., Chen, Q., & Fitzpatrick, P. (2012). Assessment of a Parametric Hurricane Surface Wind Model
840 for Tropical Cyclones in the Gulf of Mexico. In *Advances in Hurricane Research - Modelling,*
841 *Meteorology, Preparedness and Impacts*. InTech. <https://doi.org/10.5772/51288>
- 842 IOC IHO and BODC,!. (2003). *Centenary Edition of the GEBCO Digital Atlas, published on CD-ROM*
843 *on behalf of the Intergovernmental Oceanographic Commission and the International*
844 *Hydrographic Organization as part of the General Bathymetric Chart of the Oceans; British*
845 *Oceanog.*
- 846 Jelesnianski, C. P. ., Chen, J., & Shaffer, W. A. . (1992). SLOSH : Sea, Lake, and Overland Surges from
847 Hurricanes. *NOAA Technical Report, April*.
- 848 Joint Typhoon Warning Center. (2022). *Typhoon Idai (2021) Best Track Data [Data File]*. Retrieved
849 *from <https://www.metoc.navy.mil/jtwc/jtwc.html>*.
- 850 Joint Typhoon Warning Center. (2021). *Annual Tropical Cyclone Report: 2020 [PDF file]*. Retrieved
851 *from <https://www.metoc.navy.mil/jtwc/products/atcr/2020atcr.pdf>*.

Formatted: Swedish (Sweden)

- 852 Lamers, A., Devi S, S., Sharma, M., Berg, R., Gálvez, J. M., Yu, Z., Kriat, T., Cardos, S., Grant, D., &
853 Moron, L. A. (2023). Forecasting Tropical Cyclone Rainfall and Flooding Hazards and Impacts.
854 *Tropical Cyclone Research and Review*. <https://doi.org/10.1016/j.tcr.2023.06.005>
- 855 Lecacheux, S., Rohmer, J., Paris, F., Pedreros, R., Quetelard, H., & Bonnardot, F. (2021). Toward the
856 probabilistic forecasting of cyclone-induced marine flooding by overtopping at Reunion Island
857 aided by a time-varying random-forest classification approach. *Natural Hazards*, *105*(1), 227–251.
858 <https://doi.org/10.1007/s11069-020-04307-y>
- 859 Leijnse, T., van Ormondt, M., Nederhoff, K., & van Dongeren, A. (2021). Modeling compound
860 flooding in coastal systems using a computationally efficient reduced-physics solver: Including
861 fluvial, pluvial, tidal, wind- and wave-driven processes. *Coastal Engineering*, *163*, 103796.
862 <https://doi.org/https://doi.org/10.1016/j.coastaleng.2020.103796>
- 863 Liang, Q., Du, G., Hall, J. W., & Borthwick, A. G. (2008). Flood Inundation Modeling with an
864 Adaptive Quadtree Grid Shallow Water Equation Solver. *Journal of Hydraulic Engineering*,
865 *134*(11), 1603–1610. [https://doi.org/10.1061/\(ASCE\)0733-9429\(2008\)134:11\(1603\)](https://doi.org/10.1061/(ASCE)0733-9429(2008)134:11(1603))
- 866 Lin, N., Emanuel, K., Oppenheimer, M., & Vanmarcke, E. (2012). Physically based assessment of
867 hurricane surge threat under climate change. *Nature Climate Change*, *2*(6), 462–467.
868 <https://doi.org/10.1038/nclimate1389>
- 869 [Lu, P., Lin, N., Emanuel, K., Chavas, D., & Smith, J. \(2018\). Assessing hurricane rainfall mechanisms](https://doi.org/10.1175/JAS-D-17-0264.1)
870 [using a physics-based model: Hurricanes Isabel \(2003\) and Irene \(2011\). *Journal of the*](https://doi.org/10.1175/JAS-D-17-0264.1)
871 [*Atmospheric Sciences*, *75*\(7\), 2337–2358. <https://doi.org/10.1175/JAS-D-17-0264.1>](https://doi.org/10.1175/JAS-D-17-0264.1)
- 872 Luettich, R. A., Westerink, J. J., & Scheffner, N. W. (1992). ADCIRC: An Advanced Three-
873 Dimensional Circulation Model for Shelves Coasts and Estuaries, Report 1: Theory and
874 Methodology of ADCIRC-2DDI and ADCIRC-3DL, Dredging Research Program Technical
875 Report DRP-92-6. In *Coastal Engineering Research Center (U.S.), Engineer Research and*
876 *Development Center (U.S.)*. (Issue 32466, pp. 1–137). [https://erdc-](https://erdc-library.erdc.dren.mil/jspui/handle/11681/4618)
877 [library.erdc.dren.mil/jspui/handle/11681/4618](https://erdc-library.erdc.dren.mil/jspui/handle/11681/4618)
- 878 Matheson, J. E., & Winkler, R. L. (1976). Scoring Rules for Continuous Probability Distributions.
879 *Management Science*, *22*(10), 1087–1096. <https://doi.org/10.1287/mnsc.22.10.1087>
- 880 Mori, N., & Shimura, T. (2023). Tropical cyclone-induced coastal sea level projection and the
881 adaptation to a changing climate. *Cambridge Prisms: Coastal Futures*, *1*, e4.
882 <https://doi.org/10.1017/cft.2022.6>

- 883 NASA GPM. (2019). *Global Precipitation Measurement (GPM) of Cyclone Idai via*
 884 <https://gpm.nasa.gov/tropical-storm-idai-measured-gpm>. Accessed on March 16, 2023.
- 885 National Hurricane Center. (2023). *About NHC Graphics*. Retrieved June 27, 2023, from
 886 <https://www.nhc.noaa.gov/aboutnhcgraphics.shtml#WATCHWARN>.
- 887 Nederhoff, K., Giardino, A., van Ormondt, M., & Vatvani, D. (2019). Estimates of tropical cyclone
 888 geometry parameters based on best track data. *Natural Hazards and Earth System Sciences*,
 889 *19*(11), 2359–2370. <https://doi.org/10.5194/nhess-19-2359-2019>
- 890 Nederhoff, K., Hoek, J., Leijnse, T., van Ormondt, M., Caires, S., & Giardino, A. (2021). Simulating
 891 synthetic tropical cyclone tracks for statistically reliable wind and pressure estimations. *Natural*
 892 *Hazards and Earth System Sciences*, *21*(3), 861–878. <https://doi.org/10.5194/nhess-21-861-2021>
- 893 [Nederhoff, K., & van Ormondt, M. \(2023\). Tropical Cyclone Forecasting Framework: TC-FF. Zenodo.](https://doi.org/10.5281/zenodo.10433070)
 894 <https://doi.org/10.5281/zenodo.10433070>
- 895 [Neumann, B., Vafeidis, A. T., Zimmermann, J., & Nicholls, R. J. \(2015\). Future coastal population](https://doi.org/10.1371/journal.pone.0118571)
 896 [growth and exposure to sea-level rise and coastal flooding - A global assessment. PLoS ONE,](https://doi.org/10.1371/journal.pone.0118571)
 897 [10\(3\). https://doi.org/10.1371/journal.pone.0118571](https://doi.org/10.1371/journal.pone.0118571)
- 898 Nguyen, D. T., & Chen, S. T. (2020). Real-time probabilistic flood forecasting using multiple machine
 899 learning methods. *Water (Switzerland)*, *12*(3), 1–13. <https://doi.org/10.3390/w12030787>
- 900 OCHA, U. (n.d.). https://www.unocha.org/sites/unocha/files/CycloneIdai_BusinessGuide_vFinal.pdf.
- 901 Rappaport, E. N. (2014). Fatalities in the united states from atlantic tropical cyclones: New data and
 902 interpretation. *Bulletin of the American Meteorological Society*, *95*(3), 341–346.
 903 <https://doi.org/10.1175/BAMS-D-12-00074.1>
- 904 Resio, D. T., & Irish, J. L. (2015). Tropical Cyclone Storm Surge Risk. *Current Climate Change*
 905 *Reports*, *1*(2), 74–84. <https://doi.org/10.1007/s40641-015-0011-9>
- 906 Roberts, M. J., Camp, J., Seddon, J., Vidale, P. L., Hodges, K., Vannière, B., Mecking, J., Haarsma, R.,
 907 Bellucci, A., Scoccimarro, E., Caron, L. P., Chauvin, F., Terray, L., Valcke, S., Moine, M. P.,
 908 Putrasahan, D., Roberts, C. D., Senan, R., Zarzycki, C., ... Wu, L. (2020). Projected Future
 909 Changes in Tropical Cyclones Using the CMIP6 HighResMIP Multimodel Ensemble. *Geophysical*
 910 *Research Letters*, *47*(14), 1–12. <https://doi.org/10.1029/2020GL088662>
- 911 [Rye, C. J., & Boyd, J. A. \(2022\). Downward Counterfactual Analysis in Insurance Tropical Cyclone](https://doi.org/10.1007/978-3-031-08568-0_9)
 912 [Models: A Miami Case Study. 207–232. https://doi.org/10.1007/978-3-031-08568-0_9](https://doi.org/10.1007/978-3-031-08568-0_9)

Formatted: Dutch (Netherlands)

Formatted: Dutch (Netherlands)

Formatted: Dutch (Netherlands)

Field Code Changed

- 913 Roy, C., & Kovordányi, R. (2012). Tropical cyclone track forecasting techniques — A review.
 914 *Atmospheric Research*, 104–105, 40–69. <https://doi.org/10.1016/j.atmosres.2011.09.012>
- 915 Schwerdt, R. W., Ho, F. P., & Watkins, R. R. (1979). Meteorological criteria for standard project
 916 hurricane and probable maximum hurricane wind fields. *Gulf and East Coasts of the United States*.
 917 *NOAA Tech. Rep. NWS 23*, 317.
- 918 Suh, S. W., Lee, H. Y., Kim, H. J., & Fleming, J. G. (2015). An efficient early warning system for
 919 typhoon storm surge based on time-varying advisories by coupled ADCIRC and SWAN. In *Ocean*
 920 *Dynamics* (Vol. 65, Issue 5). <https://doi.org/10.1007/s10236-015-0820-3>
- 921 Taylor, A., & Glahn, B. (2008). Probabilistic guidance for hurricane storm surge. *Proc. 88th AMS*
 922 *Annual Meeting*, 8. <https://ams.confex.com/ams/pdfpapers/132793.pdf>
- 923 [Trenberth, K. E., Dai, A., Rasmussen, R. M., & Parsons, D. B. \(2003\). The Changing Character of](#)
 924 [Precipitation. *Bulletin of the American Meteorological Society*, 84\(9\), 1205–1218.](#)
 925 <https://doi.org/10.1175/BAMS-84-9-1205>
- 926 UN OCHA. (2019). *Business Guide: Cyclone Idai*. April, 1–3.
 927 <https://media.ifrc.org/ifrc/document/emergency-appeal-mozambique-cyclone-idai/>
- 928 [Van Kampen, N. G., & Reinhardt, W. P. \(1983\). Stochastic Processes in Physics and Chemistry.](#)
 929 [Physics Today](https://doi.org/10.1063/1.2915501), 36(2), 78–80. <https://doi.org/10.1063/1.2915501>
- 930 van Ormondt, M., Nederhoff, K., & Van Dongeren, A. (2020). Delft Dashboard: a quick setup tool for
 931 hydrodynamic models. *Journal of Hydroinformatics*, 22(3), 510–527.
 932 <https://doi.org/10.2166/hydro.2020.092>
- 933 Wahl, T., Jain, S., Bender, J., Meyers, S. D., & Luther, M. E. (2015). Increasing risk of compound
 934 flooding from storm surge and rainfall for major US cities. *Nature Climate Change*, 5(12), 1093–
 935 1097. <https://doi.org/10.1038/nclimate2736>
- 936 Werner, M., Schellekens, J., Gijsbers, P., van Dijk, M., van den Akker, O., & Heynert, K. (2013). The
 937 Delft-FEWS flow forecasting system. *Environmental Modelling & Software*, 40, 65–77.
 938 <https://doi.org/10.1016/j.envsoft.2012.07.010>
- 939 Wing, O. E. J., Bates, P. D., Sampson, C. C., Smith, A. M., Johnson, K. A., & Erickson, T. A. (2017).
 940 Validation of a 30 m resolution flood hazard model of the conterminous United States. *Water*
 941 *Resources Research*, 53(9), 7968–7986. <https://doi.org/10.1002/2017WR020917>

Formatted: English (United States)

Formatted: Dutch (Netherlands)

942 Yamazaki, D., Ikeshima, D., Tawatari, R., Yamaguchi, T., O'Loughlin, F., Neal, J. C., Sampson, C. C.,
943 Kanae, S., & Bates, P. D. (2017). A high-accuracy map of global terrain elevations. *Geophysical*
944 *Research Letters*, 44(11), 5844–5853. <https://doi.org/10.1002/2017GL072874>

945